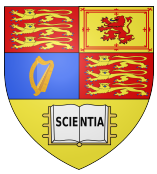

Imperial College
London

Numerical simulations of the gravitational collapse for a massless scalar field in anti-de Sitter space

Michael Meister

Supervisor

Dr Toby Wiseman

Submitted in partial fulfilment of the requirements for the degree of Master of Science of Imperial College London

September 14, 2012

Contents

1 Introduction

Regarding stars it is well known that gravitational forces contract the body, whereas outward pointing internal forces counteract this process. If the gravitational force dominates, systems with a highly compact mass can collapse and form a black hole. The point of origin is Einstein's theory of general relativity, which describes gravity as a consequence of matter and energy bending spacetime. First solutions of Einstein's field equations, the theory's fundamental equations, characterise a gravitational field of a point mass. However, the solution contains an unphysical coordinate singularity at a so-called Schwarzschild surface, which is later understood as an event horizon. Such an event horizon is a key property of black holes and has peculiar implications. E.g., in case that *any* matter touches the event horizon, it is contracted to the black hole. In the context of general relativity the black hole mass deforms the trajectory of the particle so that it is bent towards the black hole. Then the event horizon is the point of no return and once crossed, gravity is so strong such that it is impossible to avoid being contracted to the black hole centre where a singularity occurs. Once inside a black hole even light rays are prevented from escaping.

Black hole formation is an important final state of gravitational collapse, which is discussed in this dissertation for the specific case of a spherically symmetric massless scalar field. The key formulae that govern the collapse of a massless and spherically symmetric self-gravitating scalar field are Einstein's field equations

$$G_{\mu\nu} + \Lambda g_{\mu\nu} = R_{\mu\nu} - \frac{1}{2} R g_{\mu\nu} + \Lambda g_{\mu\nu} = 8\pi G T_{\mu\nu}, \tag{1.1}$$

where the energy-momentum tensor has the form

$$T_{\mu\nu} = \psi_{,\mu}\psi_{,\nu} - \frac{1}{2} g_{\mu\nu} g^{\alpha\beta} \psi_{,\alpha}\psi_{,\beta}\,. \tag{1.2}$$

Energy conservation or the contracted Bianchi identities yield the corresponding scalar field equation

$$\Box\psi = 0. \tag{1.3}$$

These equations occur throughout this dissertation and are solved using numerical schemes. The character of the field evolution depends on a critical parameter which identifies the strength of the initial field. This could for example either be the width or the amplitude of the initial curve. While the scalar field eventually disperses for weak amplitudes $p < p^*$, strong initial fields with $p > p^*$ finally form a black hole. Consequently, p^* is referred to as *critical parameter* or black hole threshold amplitude. We focus on simulations at criticality to reveal *critical phenomena* that

occur in this limit. Universality, i.e. that field evolutions at late times are independent of initial data, and universal scaling behaviour are explored. The latter phenomenon means that physical quantities like the black hole mass only depend on the deviation from the black hole threshold in the following way:

$$m_{BH} \propto (p - p^*)^\gamma \tag{1.4}$$

The scaling exponent γ is also universal. In particular, its numerical value determined by fine-tuning of initial amplitudes agrees with the value obtained from a theoretical *construction* of the critical solution.

Before revealing the structure of this dissertation, we point out that large parts discuss gravitational collapse in anti-de Sitter space. AdS_{d+2}, a hypersurface embedded in d+3 dimensional flat space $\mathbb{R}^{2,d+1}$ with metric

$$ds^2 = -dX_0^2 - dX_{d+2}^2 + \sum_{i=1}^{d+1} dX_i^2, \tag{1.5}$$

is the maximally symmetric solution of Einstein's equations with *negative* cosmological constant. A representation of AdS_{d+2} is the hyperboloid

$$-X_0^2 - X_{d+2}^2 + \sum_{i=1}^{d+1} X_i^2 = -R^2. \tag{1.6}$$

AdS_{d+2} has peculiar geometric properties, which have significant implications on collapse simulations. E.g., light rays can reach the timelike AdS boundary in finite proper time. Even though a negative cosmological constant is not observed in reality, we have recently seen growing interest in asymptotically anti-de Sitter spaces. Primary reason is Maldacena's $\mathrm{AdS}_{d+2}/\mathrm{CFT}_{d+1}$ correspondence [26], which proposes to describe a quantum mechanical force by a string theory living in anti-de Sitter space. In particular, it is conjectured that $\mathcal{N} = 4$ U(N) Yang-Mills theory corresponds to a ten dimensional superstring theory defined on $\mathrm{AdS}_5 \times \mathrm{S}^5$.

The content of this dissertation is somewhat split into two halves. The first few chapters discuss gravitational collapse in anti-de Sitter space. The difficulty of the content limits parts of the discussion to a literature review only. Any performed computations are based on numerical data supplied externally. However, the second half is a more self-contained work. As the title of this dissertations suggests concrete simulations, we implement a code for the spherically symmetric collapse of a massless scalar field in MATLAB and discuss the results. The details of the structure are as follows.

We begin with a theoretical but also descriptive introduction to critical phenomena, which gives a flavour of what to expect in concrete simulations at criticality. Building on those results, the construction of Choptuik's critical solution (for $\Lambda = 0$) as proposed by Gundlach is discussed. The idea is to impose symmetries and other characteristics expected at criticality on the solution of Einstein's field equations. This leads to hyperbolic boundary value problem which is then solved numerically. The approach in the remaining chapters is qualitatively different. We again explore

a collapse of a massless scalar field, particularly at criticality, but by fine-tuning of the amplitude of initial data. In addition, a negative cosmological constant is assumed. Since peculiar boundary properties of anti-de Sitter space play an important role in AdS collapse, the geometry of AdS is discussed first. After briefly quoting the numerical scheme, we explore critical phenomena. In particular, theoretical predictions like universality and scale invariance are reviewed. After this, we finish the first half of the dissertation with studying stability properties of a gravitational collapse in AdS. From now on, we focus on a collapse in Minkowski space. As a preparation for the understanding of the self-written code, we provide a summary for numerical methods aimed at individuals without any previous experience in numerical mathematics. Basic ideas such as numerical integration and differentiation are explained. The starting point on solving the collapse is then as before, except for a vanishing cosmological constant. However, the content is presented in a different way. In particular, we place importance on explaining the algorithm, a second-order predictor-corrector method. Regarding results, we mainly focus on critical phenomena, but also answer on what happens if matter-geometry coupling is switched off.

2 Critical phenomena

Choptuik's studies [9, 10] of the spherically symmetric collapse of a massless scalar field revealed three surprising results in regions close to the black hole threshold p^*, which are referred to as critical phenomena. First of all, the field evolution in this limit is *universal*; this means that the late time solution is independent of initial data (c.f. figure 2.12). The second phenomenon is *scale invariance* (also known as self-similarity) and means that certain physical quantities obey a periodic behaviour. More specifically, Choptuik reported an infinite number of "echoes" for precisely critical field configurations. Finally in strong field regions, these scale-invariant quantities only depend on the deviation $(p - p^*)^\gamma$ from the threshold with an exponent γ independent of initial data.

This chapter introduces critical phenomena focused on the collapse of a massless scalar field in spherical symmetry and is based on [20]. First of all, the key principle of universality is pointed out from a phase space perspective. We then provide a mathematical induction to self-similarity and the related scaling behaviour of the black hole mass m_{BH} and the maximum curvature R_{max}. For the latter phenomenon, the analogy to critical phase transitions in statistical mechanics is described.

2.1 Universality

Due to universality, the evolution of a massless scalar field in spherical symmetry can only end in either field dispersal or black hole formation. Choptuik provides evidence [9] that these two events are separated by a *critical parameter* p^*. Evolving large numbers of fields with various initial amplitudes p shows that weak configurations $p < p^*$ end in field dispersion. However, strong initial fields with $p > p^*$ eventually form a black hole. Except for the deviation $(p - p^*)^\gamma$ from the black hole threshold, the strong field evolution is independent of initial data. In this section we describe the universality phenomenon from a phase space perspective.

Each point in phase space corresponds to values for e.g. initial data, 3-metric, extrinsic curvature, and evolves in a continuous dynamical system given by Einstein's field equations. Since the final field configuration is either dispersion or black hole formation, these two phase space regions are separated by a *critical surface*. This surface contains a *critical point*, which can only be reached by a field configuration with precise amplitude p^*. Mathematically, this critical point is an attracting fixed point. The critical surface forms itself a dynamical system with one dimension less. A small deviation from it leads to an infinite number of perturbation modes tangent to the surface, which - except for *one* non-tangential growing mode - all decrease in magnitude. In principle two unstable modes are possible, but of importance in gravity is the case of a single growing mode.

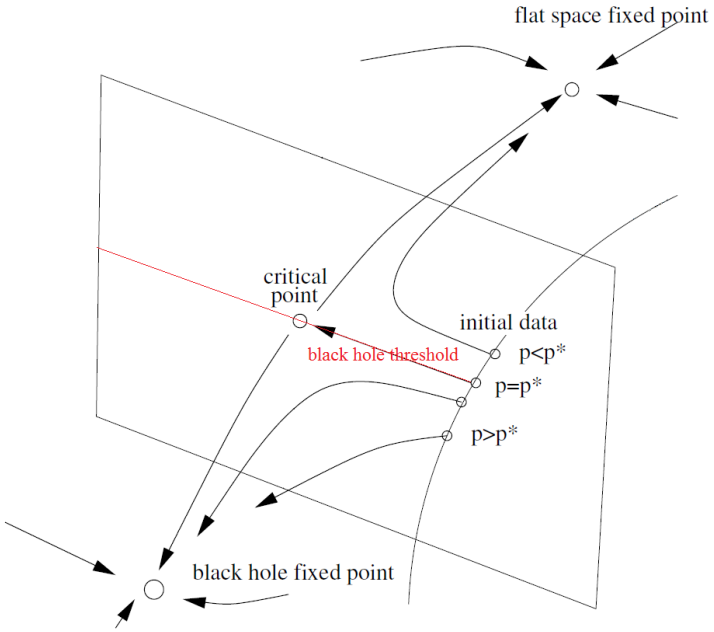

Fig. 2.1 Phase space picture depicting the critical surface that separates field dispersal from black hole formation. Lines with arrows are trajectories, whereas lines without arrows correspond to the choice of initial data (black) and the black hole threshold (red). (modified version of [20])

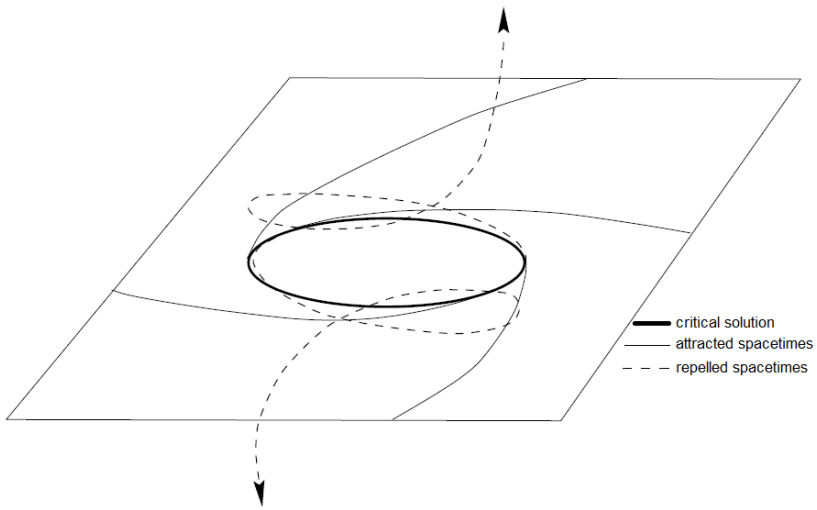

Fig. 2.11 Phase space picture for *discrete* self-similarity showing the critical solution within the critical surface. Depending on initial data, nearly critical trajectories are either attracted or repelled by the critical solution. (modified version of [18])

A simplified phase space picture of black hole formation is visualised in figures 2.1 and 2.11. We look at trajectories whose initial data are sufficiently close to the threshold value p^*. Its solution curves are attracted by the critical point and thus evolve approximately parallel to the critical surface. While precisely critical curves move towards the critical point, all other trajectories finally change direction due to the single non-tangential mode. The key point of universality is that this late time evolution is independent of the details of initial field configuration. Eventually, the trajectory only depends on the deviation $|p - p^*|$ from the threshold.

We close this section with a specific example of universality in the case of a gravitational collapse of a massless scalar field [9]. For marginally subcritical data, Choptuik evolves four different families of initial data, whose agreement at early times is increased by an overall scaling parameter. Figure 2.12 shows a universal behaviour in the sense that the profiles of the families agree with each other at late times.

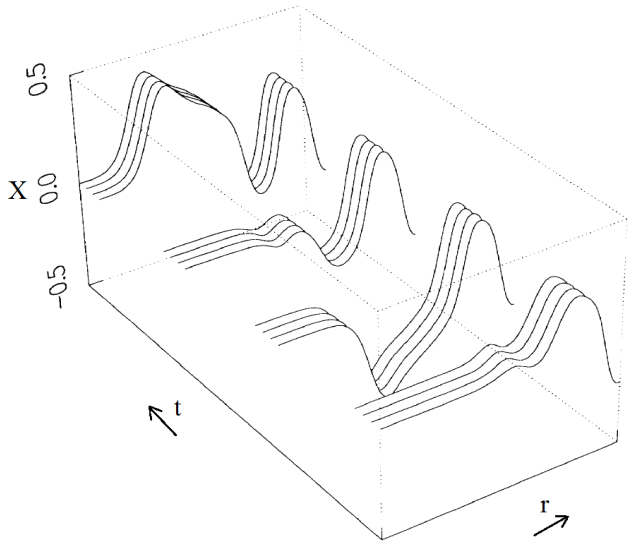

Fig. 2.12 Evolution of four different families of initial data that coincide at the beginning (foreground). Due to universality, the curves also agree with each other at late times (background). (taken from [9])

2.2 Scale invariance

The critical solution of a spherically symmetric scalar field has a *discrete* self-similarity behaviour. We introduce coordinates $x^\mu = \left(\tau, x^i\right)$ that are adapted to the symmetry. The symmetry coordinate τ is the negative logarithm of the spacetime scale, whereas x^i are the angles around the spacetime singularity. In these coordinates the metric coefficients are given by

$$g_{\mu\nu}\left(\tau, x^i\right) = e^{-2\tau}\hat{g}_{\mu\nu}\left(x^i\right). \tag{2.1}$$

The key point is that $\hat{g}_{\mu\nu}$ has a period of Δ in the τ coordinate.

In practice it is easier to work with *continuous* self-similarity, as it e.g. occurs at criticality for a spherically symmetric perfect fluid. This means that the spacetime locally obeys a continuous symmetry

$$\mathcal{L}_\xi g_{\mu\nu} = 2 g_{\mu\nu} \tag{2.2}$$

for a homothetic vector field ξ. This fixes the coordinate τ to

$$\frac{\partial}{\partial \tau} = -\xi, \tag{2.3}$$

and yields metric coefficients

$$g_{\mu\nu}\left(\tau, x^i\right) = e^{-2\tau} \hat{g}_{\mu\nu}\left(x^i\right). \tag{2.4}$$

However, various matter models include length scales that spoil scale-invariance. If this is the case, a dimensionful parameter L is introduced and it is expanded around $Le^{-\tau}$. This only works well on arbitrary small spacetime scales where length scales are negligible.

To better understand this abstract phenomenon, we again mention the collapse of a massless scalar field as a concrete example. For the strong-field evolution close to $r = 0$, Choptuik discovered that a set of scale-invariant quantities Z obeys the scaling relation [9]

$$Z^*(\rho - \Delta, \tau - \Delta) \simeq Z^*(\rho, \tau), \tag{2.5}$$

where Δ is a universal period length. This means that the same profile occurs over and over again after a time ΔT has passed by. However, the scale has to be refined by a factor of e^Δ with each recurrence in order to resolve this infinite number of "echoes".

2.3 Mass and curvature scaling

A consequence of continuous self-similarity is that near the threshold a set of scale-invariant quantities Z scales proportional to $|p - p^*|^\gamma$, where γ is a *critical exponent* independent of initial data. In this section we derive this scaling behaviour.

For $Z(x)$, a point in phase space up to an overall scale proportional to τ, $Z(x, \tau)$ is a solution trajectory, which simplifies to $Z(x, \tau) = Z^*(x)$ at the critical point p^*. We linearly perturb the solution around p^*

$$Z(x, \tau) \simeq Z^*(x) + \sum_{i=1}^{\infty} C_i(p)\, e^{\lambda_i \tau}\, Z_i(x), \tag{2.6}$$

where the expansion coefficients $C_i(p)$ are determined by initial data. Since we focus on nearly critical solutions, the phase space picture only allows a single non-tangential growing mode at late times. Thus, all coefficients except for $C_0(p)$ and the related positive real λ_0 vanish. We recap that the choice of p such that $C_0 > 0$ eventually leads to black hole formation, whereas the field finally disperses if $C_0 < 0$. In order to derive the scaling relation, equation 2.6 is rewritten in this late time limit

$$\lim_{\tau \to \infty} Z(x, \tau) \simeq Z^*(x) + \frac{dC_0}{dp}\,(p - p^*)\; e^{\lambda_0 \tau}\, Z_0(x), \tag{2.7}$$

where we also linearised around the threshold p^*. For a specific τ^* and $\epsilon \ll 1$, which retains validity of the linear expansion, we set

$$\frac{dC_0}{dp}\,(p - p^*)\,e^{-\lambda_0 \tau^*} \equiv \epsilon. \tag{2.8}$$

Reinserting into equation 2.7 yields at the point $\tau = \tau^*$

$$Z(x, \tau^*) \simeq Z^*(x) + \epsilon Z_0(x). \tag{2.9}$$

Thus, the value of Z at τ^* is universal up to an overall scale $e^{-\tau^*}$. Since $e^{-\tau^*}$ is the sole initial scale, it follows from equation 2.8 that

$$Z(x, \tau^*) \propto e^{-\tau^*}. \tag{2.10}$$

We stress that the discussion above is only valid for continuous self-similarity. For discrete self-similarity, an additional periodic structure appears on small scales. In other words a weak function $f(z)$ with period Δ is superimposed on top of the solution.

Specific examples that we encounter in this dissertation are the black hole mass scaling (c.f. figure 7.4.44)

$$m_{BH} \propto e^{-\tau^*} \propto (p - p^*)^{\frac{1}{\lambda_0}} =: (p - p^*)^{\gamma}\,, \tag{2.11}$$

and the maximum curvature scaling (c.f. figure 7.4.41)

$$R_{max} \propto (p - p^*)^{2\gamma}\,. \tag{2.12}$$

The factor of two in the exponent occurs due to the quadratic length scale of curvature. Furthermore, the horizon radius x_H in a spherical collapse in anti-de Sitter space scales near each critical amplitude ϵ_n as (c.f. figure 5.2)

$$x_H(\epsilon) \propto (\epsilon - \epsilon_n)^{\gamma}\,. \tag{2.13}$$

In addition, similar power-law scalings hold for the black hole charge Q and the angular momentum L.

2.3.1 Analogy with critical phase transitions

Universal phenomena also occur in statistical mechanics in the field of critical phase transitions. In statistical mechanics macroscopic observables A and its external forces f are described by an ensemble (a large number) of microscopic states. Statistical quantities like expectation values and variances are related to derivatives of a partition function

$$Z(\mu, f) \;=\; \sum_{\text{microstates}} e^{-H(\text{microstate},\mu,f)}. \tag{2.14}$$

The macroscopic parameters μ and f of the Hamiltonian determine the distribution. In this context, phase transitions are discontinuities in observables. A concrete example is a solid-liquid-gas phase

transition. For a fluid, the density ρ_{liquid} suddenly changes its value at a temperature T due to the phase transition from liquid to gas state. In the neighbourhood of a further increased critical temperature T^*, the density difference scales as [20]

$$\rho_{liquid} - \rho_{gas} \propto (T^* - T)^{\gamma}\,, \tag{2.15}$$

which is the same universal scaling relation as before.

The discussion of universal phenomena as it is structured in this chapter might suggest that it only applies for a spherical collapse of a massless scalar field. While Choptuik's pioneering results in this field introduced the term critical phenomena, further research for other types of matter showed that the presented ideas are general and extend far beyond spherical symmetry. E.g. even in the case of collision of two black holes, whose critical solution is a circular orbit, the number of orbits below and above the threshold obeys a scaling behaviour with a universal constant γ. This is why we refer to [20] for a more comprehensive discussion of critical phenomena. With regard to spherical symmetry, table one on page 31 provides a useful overview of previous work on critical collapse for several types of matter.

3 Critical solution

Following discovery of critical phenomena [9], we have seen growing interest in understanding this pattern. The theoretical framework was introduced in the previous chapter. This chapter, however, focuses on the *construction* of Choptuik's critical solution. The basic idea is to construct a solution for a spherically symmetric collapse of a massless scalar field by imposing discrete scale-invariance and analyticity. Gundlach covers the topic in a series of papers [17–19]. The more recent ones [18, 19] are written in much detail and describe the global structure of the critical solution. This includes, apart from revealing the structure at the past lightcone of the singularity, an extension of the solution to the future lightcone of the singularity and consequently an analysis of regularity/differentiability. Concerning the topic of this dissertation, however, a discussion of the first publication [17] is more suitable.

In this paper Gundlach constructs the critical solution of a spherical symmetric collapse of a massless scalar field. By demanding discrete scale-invariance and analyticity, the problem, governed by Einstein's equations, is reformulated as a hyperbolic boundary value problem. We discuss the derivation, but avoid describing the subtle numerical scheme used to solve it. However, we stress that the region of convergence of the algorithm is small. Thus, the scheme requires input data made available by Choptuik [9]. The obtained results then confirm Gundlach's ansatz. The value of the echoing period Δ, which is the eigenvalue of the hyperbolic boundary value problem, agrees with Choptuik's results and so does the critical exponent. In addition, a comparison of the spacetime variables shows that the critical solution improved the precision of Choptuik's spacetime by one to two orders of magnitude [17].

3.1 Construction of critical solution

A scalar field collapse in spherical symmetry is governed by Einstein's field equations

$$G_{\mu\nu} = 8\pi G\left(\phi_{,\mu}\phi_{,\nu} - \frac{1}{2}g_{\mu\nu}g^{\alpha\beta}\phi_{,\alpha}\phi_{,\beta}\right), \tag{3.1}$$

and the corresponding scalar field equation

$$\phi_{,c}{}^{,c} = 0. \tag{3.2}$$

The metric, whose gauge freedom is fixed by the condition $\alpha(t, r = 0) \equiv 1$, is chosen as proposed by Choptuik [9]:

$$ds^2 = -\alpha^2(t, r)dt^2 + a^2(t, r)dr^2 + r^2 d\Omega^2 \tag{3.3}$$

We then introduce auxiliary matter fields

$$X(t,r) = \sqrt{2\pi G}\,\frac{r}{a}\,\phi_{,r}\,, \quad Y(t,r) = \sqrt{2\pi G}\,\frac{r}{\alpha}\,\phi_{,t}. \tag{3.4}$$

Due to *discrete* scale invariance, we have a logarithmic symmetry of $Z(t,r) = Z(te^{\Delta}, re^{\Delta})$, which is simplified to a periodicity in Z by defining

$$\tau \equiv \ln(\pm t), \quad \xi \equiv \ln\left(\frac{\pm r}{t}\right). \tag{3.5}$$

This yields a symmetry of

$$Z(\tau,\xi) = Z(\tau+\Delta,\xi). \tag{3.6}$$

This discrete homotheticity can be geometrically thought of as Lie-dragging the metric alongside the vector field $\frac{\partial}{\partial\tau}$ (c.f. beginning of section 2.2). However, there is an arbitrariness in this vector field which has to be described by a periodic function $\xi_0(\tau)$. Thus, defining a new coordinate $\zeta \equiv \xi - \xi_0(\tau)$ and rescaling the time coordinate to $\varphi \equiv \frac{2\pi\tau}{\Delta}$, yields the symmetry

$$Z(\varphi,\zeta) = Z(\varphi+2\pi,\zeta). \tag{3.7}$$

Applying these definitions of variables and substituting the metric 3.3 into the field equations, leads to a set of equations which is solved for the field's ζ-derivatives. However, the equations are "messy" and hence better expressed in terms of a new field $g \equiv \frac{a}{\alpha}\,e^{\xi_0(\tau)}$ and following abbreviations:

$$X_{\pm} \equiv X \pm Y,\ z \equiv \left(1 + \frac{2\pi}{\Delta}\frac{d\xi_0}{d\varphi}\right)^{-1},\ D \equiv z^{-1}\,e^{\zeta}\,g \tag{3.8}$$

$$B_{\pm} \equiv \frac{1}{2}(1-a^2)X_{\pm} - a^2 X_{\pm}X_{\mp}^2 - X_{\mp} \pm z\frac{2\pi}{\Delta}X_{\pm,\varphi}D \tag{3.9}$$

The evolution equations then have the form of

$$a_{,\zeta} = \frac{1}{2}a[(1-a^2) + a^2(X_+^2 + X_-^2)], \tag{3.10}$$

$$g_{,\zeta} = g(1-a^2), \tag{3.11}$$

$$X_{+,\zeta} = \frac{B_+}{1+D}, \tag{3.12}$$

$$X_{-,\zeta} = \frac{B_-}{1-D}. \tag{3.13}$$

The corresponding constraint equation is

$$z\frac{2\pi}{\Delta}\frac{a_{,\varphi}}{a} = \frac{1}{2}[(1-a^2) + a^2(X_+^2 + X_-^2) + a^2D^{-1}(X_+^2 - X_-^2)]. \tag{3.14}$$

By interpreting φ as the angular coordinate in a polar coordinate system and by keeping ζ small, the equations above describe a constrained Cauchy problem. Regularity of the metric requires $a = 1$ at $(\zeta = -\infty, r = 0)$. In order to specify data obeying the conditions above, we need another free function $Y_0(\varphi)$ which is determined by the following expansion in terms of e^{ζ}:

$$Y(\varphi, \zeta) \equiv Y_0(\varphi)\, e^{\xi_0(\varphi)}\, e^{\zeta} + O(e^{3\zeta}) \tag{3.15}$$

Having assembled all the prerequisites, we aim to formulate equations 3.10-3.13 as a hyperbolic boundary value problem. As one approaches the point $D = 1$ with increasing ζ, a degeneracy occurs. This region is referred to as "sonic" line and, since radial null geodesics obey

$$\frac{d\zeta}{d\varphi} = -\frac{\Delta}{2\pi z}(-1 \pm D^{-1}), \tag{3.16}$$

it is the intersection of a null geodesic and a surface of constant ζ. However, the solution can be analytically continued beyond this sonic line by shifting it to $\zeta = 0$ and power-expanding in ζ. Regular data close to $\zeta = 0$ is then determined by $\xi_0(\varphi)$ and another free function $X_{+0}(\varphi)$

$$X_{+0}(\varphi) \equiv X(\varphi, \zeta = 0) + Y(\varphi, \zeta = 0). \tag{3.17}$$

This framework gives rise to a hyperbolic boundary value problem on a rectangle, whose two sides are identified by a cylinder. After choosing three independent fields, e.g. g, X_+ and X_-, a count of degrees of freedom suggests a locally unique solution.

Gundlach solved this problem numerically using pseudo-spectral and relaxation methods [28]. However, since we do not implement his algorithm, we waive a discussion and refer to [17, 18]. Instead of that we find it more important to discuss input data and results. Trial simulations indicate a small region of convergence. As a consequence, any input data has to be sufficiently close to the critical solution to ensure convergence. Since Gundlach aims to construct Choptuik's critical solution, it is obvious to set any input data to Choptuik's numerical results for a nearly critical collapse. More specifically, Choptuik provided initial data [11]

$$Y_0 = -2.3 \sin\varphi \; - 0.6 \sin 3\varphi, \quad \Delta = 3.44. \tag{3.18}$$

Before quoting any results, we once again stress the difference between Choptuik's pioneer work [9, 10] and Gundlach's papers [17–19]. While Choptuik solves a collapse of a spherically symmetric scalar field by fine-tuning of Cauchy-data, Gundlach imposes symmetries found by Choptuik and constructs the critical solution as a hyperbolic boundary value problem, which is then solved numerically. The results confirm this ansatz to find the critical solution. According to table 1 in [17] the solution's echoing period is determined to $\Delta = 3.4439 \pm 0.0004$. This result does not only agree with [9, 10], but it is more accurate and thus has a smaller error estimate. More specifically, a comparison of the fields a, α, X, and Y shows that Gundlach's construction of the critical solution improved the precision of Choptuik's spacetime by one to two orders of magnitude [17].

3.2 Critical exponent

In this section the critical exponent γ is determined by using Gundlach's construction of the critical solution. The ansatz is as in section 2.3, except for an adapted coordinate system. We interpret Z as a shorthand notation for (a, X_+, X_-, g) and then linearly perturb the critical solution to get

$$\delta Z(\tau, \zeta) = \sum_{i=1}^{\infty} C_i \, e^{\lambda_i \tau} \, \delta_i Z(\tau, \zeta), \tag{3.19}$$

where the expansion coefficients C_i are given by initial data. The range of the complex frequencies of the modes λ_i is limited to $0 \leq \operatorname{Im} \lambda_i < \frac{\pi}{\Delta}$. It is important that the perturbation ansatz 3.19 breaks discrete homotheticity such that δZ no longer obeys this symmetry. However, homotheticity with period Δ of each *single* mode remains unbroken.

In order to determine the critical exponent, the variation of Z is expanded to yield an equation for each component $\delta_i a$, $\delta_i X_\pm$, $\delta_i g$. The idea is to start with

$$\delta Z_{,\zeta} = A \, \delta Z + B \, \delta Z_{,\tau}, \tag{3.20}$$

which then leads to an equation for $\delta_i Z$:

$$\delta_i Z_{,\zeta} = (A + \lambda_i B) \, \delta_i Z + B \, \delta_i Z_{,\tau} \tag{3.21}$$

The resultant equations are tedious, as is the numerical method used to solve it. This is why we refer to [17] for those details. Instead of that we better focus on results.

Since we are analysing scaling behaviour at criticality, we are interested in growing modes close to the singularity at $\tau = -\infty$. This limits frequencies to the left half plane of λ_i. As already described in section 2.3, from a phase space perspective only a single non-tangential growing mode is expected, whereas all other modes should decrease and become irrelevant. Numerical results [17, 18] indeed confirm this. More specifically, the frequency of the unique growing mode is $\lambda_0 = -2.674 \pm 0.009$. Its reciprocal value determines the critical exponent to $\gamma = 0.374 \pm 0.001$, which numerically agrees on all digits beyond the decimal point with the most accurate value [21] experimentally found so far.

In summary, success of the critical solution is connected to Choptuik's discovery of critical phenomena. By imposing the newfound discrete symmetry, a hyperbolic boundary value problem is constructed and then numerically solved. Owing to a small region of convergence, this requires an estimation [9] of the period Δ and the free function Y_0 as input. The critical solution's values of both the echoing period Δ and the scaling exponent γ numerically agree with the values obtained by fine-tuning of initial data. In particular, precision of knowledge of the Choptuik spacetime is increased by one to two orders of magnitude.

4 Collapse in anti-de Sitter space

In this chapter we explore gravitational collapse in anti-de Sitter space. Until recently simulations were only performed in 2+1 dimensions and entirely focused on solutions *before* any reflection off the boundary [29]. The remaining features are treated on its own in chapter 5.

The structure is as follows. After an introduction to Einstein's equations, we recap important features of the geometry of AdS. We then quote metric and evolution equations, which also includes a discussion of initial and regularity conditions. Since no concrete simulation is performed in this chapter, the numerical scheme - except for singularity excision - is only briefly mentioned. Therefore, we place more importance on results. As proposed in chapter 2, we find a scaling behaviour with a universal exponent γ. Furthermore, it is pointed out why the associated mass scaling in AdS is difficult to measure. As a consequence, the maximum Ricci curvature scalar is used instead to determine γ. After introducing self-similarity adapted coordinates, we observe the field's second derivative in terms of those. It turns out that the profiles of Gaussian, Gaussian-squared and kink initial data are indistinguishable in the critical limit.

4.1 Introduction

Einstein's equations in 2+1 dimensions for a circularly symmetric massless scalar field with cosmological constant $\Lambda \equiv -\frac{1}{l^2}$ are

$$G_{\mu\nu} + \Lambda g_{\mu\nu} = R_{\mu\nu} - \frac{1}{2} g_{\mu\nu} R + \Lambda g_{\mu\nu} = 4\pi T_{\mu\nu}. \tag{4.1}$$

The scalar field's energy-momentum tensor is

$$T_{\mu\nu} = \phi_{,\mu}\phi_{,\nu} - \frac{1}{2} g_{\mu\nu} g^{\alpha\beta}\phi_{,\alpha}\phi_{,\beta}. \tag{4.2}$$

Its orbitally symmetric field equation is given by

$$\Box\phi = 0. \tag{4.3}$$

Since we focus on a non-rotating collapse, the scalar field only depends on radial r and time t coordinate in symmetry-adapted coordinates (r, t, θ). Before quoting metric and evolution equations, we find it important to discuss the geometry of anti-de Sitter space. Some of its geometric features, especially causal structure and boundary properties, are peculiar and require special treatment. Hence, basic knowledge of AdS geometry is essential before we go any further.

4.1.1 Geometry of AdS

This section is based on [1, 4] and reviews the geometry of AdS in order to prepare for a simulation of a gravitational collapse. Key properties of AdS, e.g. that light rays, as seen by an observer on a geodesic, travel to and bounce off the timelike boundary in finite proper time, are only understood after discussing AdS geometry. Apart from acting as a preparation for later chapters, geometric features of the AdS/CFT correspondence are pointed out. Even though the actual correspondence (refer to [1]) is not included in this dissertation, it is important to motivate the conjecture from a geometric point of view; particularly because the origins of research in AdS dynamics lie in this correspondence.

We begin by discussing conformal structure of Minkowski space to eventually point out that the isometry group of AdS_{d+2} is the conformal symmetry of flat space $\mathbb{R}^{1,d}$. It is further shown that a conformal transformation maps a half plane of $\mathbb{R}^{1,d}$ into a triangular region, whose maximally extended space has the geometry $\mathbb{R} \times \mathrm{S}^d$ of the Einstein static universe. We then define AdS space, discuss its properties and find that the conformal compactification of AdS has the geometry of *one half* of the Einstein static universe, where its dimension is higher by one than in the flat space case. In conclusion, the boundary of the conformal compactification of AdS_{d+2} equals the conformally compactified $\mathbb{R}^{1,d}$ space, which is a key point in the $\mathrm{AdS}_{d+2}/\mathrm{CFT}_{d+1}$ correspondence.

Conformal transformation

A conformal transformation is a change of a physical metric ds^2 by a factor $\Omega \in \mathbb{R}$ which then yields an unphysical metric

$$ds'^2 = \Omega^2 ds^2. \tag{4.4}$$

Since the sign of a vector's norm does not change under such a transformation, causal structure, i.e. the notion of timelike and spacelike, is invariant. We are dealing with infinite spaces and thus conformal transformations that compactify these spaces such that the boundaries are mapped to finite distance are of particular interest. A first example is two-dimensional Minkowski space $\mathbb{R}^{1,1}$.

Minkowski space

The two-dimensional Minkowski metric is

$$ds^2 = -dt^2 + dx^2, \qquad -\infty < t, x < \infty. \tag{4.5}$$

We conformally map $\mathbb{R}^{1,1}$ into a (compact) rectangle (c.f. figure 4.1.1) by a series of coordinate transformations

$$ds^2 = -dudv = \frac{1}{4\cos^2\hat{u}\cos^2\hat{v}}\left(-d\tau^2 + d\theta^2\right), \tag{4.6}$$

where we changed variables ($u = t - x, v = t + x$) in the first and ($u = \tan\hat{u}, v = \tan\hat{v}; \hat{u} = \frac{\tau-\theta}{2}, \hat{v} = \frac{\tau+\theta}{2}$) in the second step. The former spatial infinities $x = \pm\infty$ are mapped to finite distance at the corners of a rectangle ($\tau = 0, \theta = \pm\pi$). We refer to any conformally compactified space with same boundary structure as *asymptotically flat* spacetime.

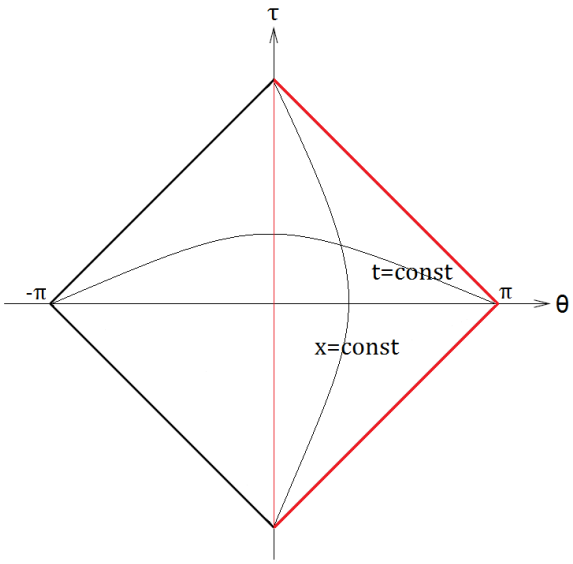

Fig. 4.1.1 The conformal compactification of two-dimensional Minkowski space in (τ, θ) coordinates is a rectangle. The (t, r) half plane of higher-dimensional Minkowski space is conformally mapped into the red triangle.

For higher-dimensional Minkowski space $\mathbb{R}^{1,d}$, the physical metric in spherical coordinates is

$$ds^2 = -dt^2 + dr^2 + r^2 d\Omega_{d-1}^2, \tag{4.7}$$

where $d\Omega_{d-1}^2$ is the line element of the d-1 sphere. As before, a similar series of coordinate transformations yields

$$ds^2 = \frac{1}{4\cos^2\hat{u}\cos^2\hat{v}}\left(-d\tau^2 + d\theta^2 + \sin^2\theta\, d\Omega_{d-1}^2\right). \tag{4.8}$$

Since this metric diverges at either $\hat{u} = \frac{\pi}{2}$ or $\hat{v} = \frac{\pi}{2}$, we multiply by a conformal factor Ω which vanishes at the boundary as it is required. This yields the unphysical metric

$$ds'^2 = -d\tau^2 + d\theta^2 + \sin^2\theta\, d\Omega_{d-1}^2, \tag{4.9}$$

which again has same causal structure. We are interested in its maximal extension, so the conformally scaled metric is analytically extended to

$$0 \leq \theta \leq \pi, \quad -\infty < \tau < \infty. \tag{4.10}$$

If we further identify the points $(\tau = 0, \theta = 0)$ and $(\tau = 0, \theta = \pi)$ with the poles of S^d, then the geometry of the extended space is $\mathbb{R} \times S^d$ and therefore equals the Einstein static universe. In particular, the maximally compact subgroup SO(2) × SO(d+1) of the conformal SO(2,d+1) group of $\mathbb{R}^{1,d}$ is the isometry of the Einstein static universe.

Anti-de Sitter space

AdS_{d+2} is a hypersurface in d+3 dimensional flat space $\mathbb{R}^{2,d+1}$ with metric

$$ds^2 = -dX_0^2 - dX_{d+2}^2 + \sum_{i=1}^{d+1} dX_i^2. \tag{4.11}$$

AdS_{d+2} is then defined by

$$-X_0^2 - X_{d+2}^2 + \sum_{i=1}^{d+1} X_i^2 = -R^2, \tag{4.12}$$

which is a hyperboloid (c.f. figure 4.1.11). To derive the AdS metric, we find that the following parameterisation (so-called global coordinates on AdS) solves equation 4.12

$$\begin{aligned} X_0 &= R\cosh r\cos\tau, \\ X_{d+2} &= R\cosh r\sin\tau, \\ X_i &= R\sinh r\ \Omega_i, \qquad\qquad \sum_i \Omega_i^2 = 1, \end{aligned} \tag{4.13}$$

where $r \geq 0$ and $0 \leq \tau < 2\pi$. Substituting these global coordinates into 4.11 yields the AdS_{d+2} metric

$$\begin{aligned} ds^2 &= R^2\left(-\cosh^2 r\, d\tau^2 + dr^2 + \sinh^2 r\, d\Omega^2\right) \\ &= R^2\sec^2\theta\left(-d\tau^2 + d\theta^2 + \sin^2\theta\, d\Omega^2\right), \end{aligned} \tag{4.14}$$

where we changed coordinates $\sinh r = \tan\theta$ which limits the range of θ to $0 \leq \theta \leq \frac{\pi}{2}$.

Since the AdS hyperboloid has the geometry $\mathrm{S}^1 \times \mathbb{R}^{d+1}$, its topology is not simply connected. In particular, since S^1 represents a closed curve in time direction (c.f. figure 4.1.11), the spacetime is not causal. Thus, we have to decompactify the τ coordinate to $-\infty < \tau < \infty$ to remove closed timelike curves. So from now on, we regard this *universal cover* of AdS instead of AdS itself.

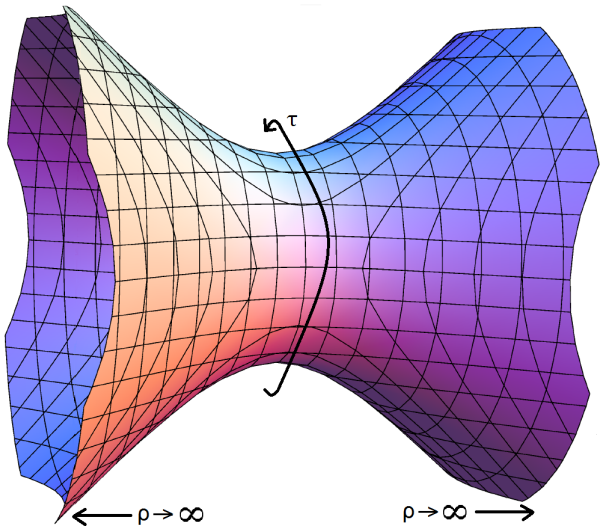

Fig. 4.1.11 AdS_2 is a one-sheeted hyperboloid in $\mathbb{R}^{2,1}$. Due to closed timelike curves along τ, we usually unwrap it along the closed circle to allow proper causal structure. This is referred to as universal cover of AdS.

The isometry group of AdS_{d+2} is SO(2,d+1) and has the maximally compact subgroup SO(2) $\times$ SO(d+1). The symmetry properties again resemble the ones of the Einstein static universe. To investigate this further, we already have transformed the AdS_{d+2} metric to θ coordinates in equation 4.14. Conformally rescaling yields

$$ds'^2 = -d\tau^2 + d\theta^2 + \sin^2\theta\, d\Omega^2, \tag{4.15}$$

where we stress that the *limited* range of θ is $0 \leq \theta < \frac{\pi}{2}$. Thus, the conformal compactification of AdS corresponds to *one half* of the Einstein static universe. Comparing to conformally compactified Minkowski space, the dimension of the Einstein static universe related to AdS is one dimension higher. It turns out that the *boundary* of the conformal compactification of AdS_{d+2} equals the conformally compactified Minkowski space $\mathbb{R}^{1,d}$. The AdS_{d+2}/CFT_{d+1} correspondence is based on this relationship and we again refer to [1] for a detailed discussion.

We finish this section with a remark about boundary properties of the AdS geometry. The boundary C at $\theta = \frac{\pi}{2}$ is a timelike surface, which is quite different from what we are used to work with. In particular, interior and boundary behaviour are not related. In other words information is consistently entering from this timelike boundary. As a consequence, it is not possible to evolve the solution on a specific time slice to the whole future. The Cauchy problem on AdS is therefore not well-posed unless we set boundary conditions on the timelike $\theta = \frac{\pi}{2}$ boundary.

4.1.2 Metric and evolution equations

As just discussed, the geometry of AdS has unusual properties which make numerical simulations of a gravitational collapse in 2+1 dimensional anti-de Sitter space more challenging. E.g., the

timelike null infinity surface C demands for Dirichlet conditions for the scalar field ϕ. It turns out that a reasonable choice of metric is [29]

$$ds^2 = \frac{e^{2A(r,t)}}{\cos^2(r/l)}\left(dr^2 - dt^2\right) + l^2\tan^2(r/l)\, e^{2B(r,t)}\, d\theta^2. \tag{4.16}$$

Owing to the symmetry, the metric functions $A(r,t)$ and $B(r,t)$ only depend on radial r and time t coordinate. The singularity of the metric at null infinity ($r = \frac{\pi l}{2}$) is cured by choosing values of A and B on C such that the space asymptotically equals anti-de Sitter. Obviously, the metric solves Einstein's equations 4.1 for $T_{\mu\nu} = 0$ if we set $A = B = 0$. Using this metric and defining gradients $\Phi(r,t) = \phi_{,r}$ and $\Pi(r,t) = \phi_{,t}$ of the scalar field, Einstein's field equations expand into

$$-A_{,tt} + A_{,rr} + \frac{1 - e^{2A}}{l^2\cos^2(r/l)} + 2\pi\left(\Phi^2 - \Pi^2\right) = 0, \tag{4.17}$$

$$-B_{,tt} + B_{,rr} - B_{,t}^2 + B_{,r}\left(B_{,r} + \frac{2}{l\cos(r/l)\sin(r/l)}\right) + \frac{2\left(1 - e^{2A}\right)}{l^2\cos^2(r/l)} = 0, \tag{4.18}$$

$$\begin{aligned} B_{,rr} - A_{,t}B_{,t} + B_{,r}\left(B_{,r} - A_{,r} + \frac{1 + \cos^2(r/l)}{l\cos(r/l)\sin(r/l)}\right) + \\ + \frac{1 - e^{2A}}{l^2\cos^2(r/l)} - \frac{A_{,r}}{l\cos(r/l)\sin(r/l)} + 2\pi\left(\Phi^2 + \Pi^2\right) = 0, \end{aligned} \tag{4.19}$$

$$B_{,tr} - A_{,t}\left(B_{,r} + \frac{1}{l\sin(r/l)\cos(r/l)}\right) + B_{,t}\left(B_{,r} - A_{,r} + \frac{\cot(r/l)}{l}\right) + 4\pi\Phi\Pi = 0. \tag{4.20}$$

The Ricci curvature scalar has the form

$$R = \frac{4\pi\cos^2(r/l)}{e^{2A}\, l^2}\left(\Phi^2 - \Pi^2\right) - \frac{6}{l^2}. \tag{4.21}$$

While the former two field equations describe the evolution, the latter two characterise constraints. Since we only have to determine two unknown variables, it is sufficient to solve for A and B in 4.17 and 4.18. Equations 4.19 and 4.20 are then used to monitor the error. The set is completed by the scalar field equation

$$\left(\tan(r/l)\, e^B\, \Phi\right)_{,r} - \tan(r/l)\left(\Pi\, e^B\right)_{,t} = 0. \tag{4.22}$$

Regularity and initial conditions for the equations are quoted in connection with the numerical scheme. Both of which is discussed in the next section.

4.2 Numerical scheme

We aim to keep this section brief, primarily because we do not perform any concrete simulations. We quote the numerical scheme together with its initial and regularity conditions used in [29] and

highlight numerical challenges that Pretorius and Choptuik have experienced. Finally, detecting black holes and consequently excising singularities is discussed in more detail[1].

The subset 4.17 and 4.18 of Einstein's equations and the scalar field equation 4.22 are finite-differenced on a uniform grid and then solved by a second-order predictor-corrector method. The number of grid points is chosen such that the Courant factor is 0.1. The integration moves from $r = 0$ outwards, initially $A_{,t}(0,0) = 0$. It turns out that high-frequency components and solutions close to the boundary at $r = \frac{\pi l}{2}$ are numerically challenging [29]. While the former is resolved by Kreiss-Oliger dissipation [25], instabilities in proximity to the boundary spread out and lead to failures in the black hole formation process. Pretorius and Choptuik fixed this issue by using higher-order finite-differencing (6-point 4^{th}-order approximation) and by solving for the metric value A in equation 4.20 (instead of 4.17 and 4.18) in the second to last step before the boundary.

4.2.1 Initial and regularity conditions

The system of equations 4.17, 4.18 and 4.22 requires initial conditions for $\Phi(r,0)$, $\Pi(r,0)$, $B(r,0)$ and $B_{,t}(r,0)$ in order to solve numerically for $A(r,0)$ and $A_{,t}(r,0)$. Since we consider evolutions without any trapped surfaces, we can set $B_{,t}(r,0) = B(r,0)$. To confirm that critical phenomena are independent of the family of the initial field, we examine the collapse of an ingoing n^{th} power Gaussian curve (c.f. figure 4.2.1)

$$\phi(r,0) = Pe^{((r-r_0)/\sigma)^{2n}}, \tag{4.23}$$

and an ingoing kink-like curve with gradient

$$\frac{\partial\phi}{\partial r}(r,0) = \frac{-2P\sqrt{\sigma}\sin(r/l)\cos(r/l)\left(2(r-r_0)(1-2\sin^2(r/l)) - l\sin(r/l)\cos(r/l)\right)}{\pi l\left(\sigma\sin^4(r/l)\cos^4(r/l) + (r-r_0)^2\right)}e^{-(r-r_0)^2/\sigma^2}. \tag{4.24}$$

[1] This subsection is covered in more detail because excision strategies are not contained in the self-written code (c.f. chapter 7) and thus do not occur again in this dissertation.

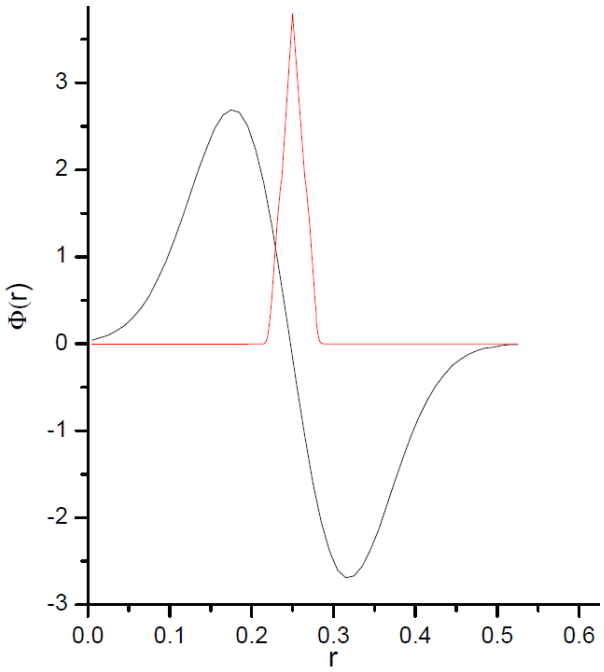

Fig. 4.2.1 Gradient $\Phi(r,0) = \phi_{,r}(r,0)$ for Gaussian (black) and kink-like (red) initial data centered around $r = 0.25$.

Regularity of $A(r,t)$, $B(r,t)$, $\Phi(r,t)$ and $\Pi(r,t)$ at $r = 0$ and $r = \frac{\pi l}{2}$ requires the following Dirichlet and Neumann boundary conditions:

$$A_{,t}(0,t) = B_{,t}(0,t), \qquad A_{,t}\left(\frac{\pi l}{2},t\right) = A\left(\frac{\pi l}{2},t\right) = 0, \tag{4.25}$$

$$A_{,r}(0,t) = 0, \qquad A_{,r}\left(\frac{\pi l}{2},t\right) = A\left(\frac{\pi l}{2},t\right) = 0, \tag{4.26}$$

$$B_{,r}(0,t) = 0, \qquad B_{,r}\left(\frac{\pi l}{2},t\right) = 0, \tag{4.27}$$

$$\Phi(0,t) = 0, \qquad \Phi\left(\frac{\pi l}{2},t\right) = 0, \tag{4.28}$$

$$\Pi_{,r}(0,t) = 0, \qquad \Pi\left(\frac{\pi l}{2},t\right) = 0. \tag{4.29}$$

Variables A and B are overdetermined and thus not all of the constraints above have to be implemented. A possible choice (as in [29]) is to place Neumann boundary conditions at the origin and Dirichlet conditions at the C boundary. The remaining constraints are then checked for consistency.

4.2.2 Singularity excision

For supercritical initial data, a spacelike [7] curvature singularity forms inside an apparent horizon. Eventually, diverging metric variables cause the simulation to fail. Whilst black hole excision techniques cut out significant regions inside the event horizon, singularity excision only removes the causal future of the singularity and thus resolves its surrounding structure.

Developing black holes are indicated by the formation of trapped surfaces, which occur if

$$1 + l \sin(r/l) \cos(r/l) \, (B_{,r} + B_{,t}) < 0. \tag{4.30}$$

At the apparent horizon, the black hole mass m_{BH} can be estimated from a general mass aspect function $M(r, t)$, which is derived from the BTZ metric

$$ds^2 = -\left(\frac{\hat{r}^2}{l^2} - M\right) d\hat{t}^2 + \frac{1}{\hat{r}^2/l^2 - M^2} d\hat{r}^2 + \hat{r}^2 d\theta^2. \tag{4.31}$$

In these coordinates the mass M is defined by

$$|\nabla \hat{r}|^2 \equiv \frac{\hat{r}^2}{l^2} - M(\hat{r}, \hat{t}). \tag{4.32}$$

Switching back to (r, t) coordinates, 4.32 yields

$$M(r,t) = \left(\tan^2(r/l) e^{2A} + l^2 \sin^2(r/l)(B_{,t}^2 - B_{,r}^2) - 2l \tan(r/l) B_{,r} - \sec^2(r/l)\right) e^{2(B-A)}. \tag{4.33}$$

Eventually, the black hole mass m_{BH} at the apparent horizon r_{AH} is approximated by

$$m_{BH} \approx \tan^2(r_{AH}/l) \, e^{2B(r_{AH}, t)}. \tag{4.34}$$

Equation 4.34 will later be useful to confirm the scaling behaviour of the black hole mass.

If black hole formation is detected, the values of the metric variables have to be carefully observed. Once those exceed a critical threshold, the simulation breaks down unless singularity excision is implemented: Removing grid points, whose metric variables are sufficiently large, together with its direct surroundings (~ 5 grid points) avoids an otherwise imminent crash. At the boundary, finite-differenced operators have to be either adapted forward or backward to become independent of the excised region. In addition, we remove the *unphysical* causal future of the excised region. In theory multiple excised zones are possible, but in 2+1 dimensional AdS collapse it is sufficient to cut out one region. Depending on choice of coordinates and metric, it can be challenging to implement singularity excision. However, owing to conventions used in [29], this is relatively simple. E.g., since radial null curves have constant speed, the excised causal future expands by one grid point per time step. Anyway, a check that should be done on any singularity excision scheme is to ensure that evolutions with a single excised light cone yield the regular solution for small r.

4.3 Results

The results [29] of a 2+1 dimensional collapse in AdS mainly focus on the black hole threshold *before* any reflection off the C boundary. After a brief introduction on how to locate the threshold, we explore the mass behaviour in terms of the initial field amplitude p. Of particular interest is to demonstrate universal scaling behaviour. However, it turns out that mass scaling only yields an estimation of the value of the scaling exponent. Since it is more accurate, the maximum Ricci curvature scalar R_{max} is used to determine the exponent γ. We further discuss critical phenomena by showing that the field function $\Phi(Z, T)$ in the critical limit, where (Z, T) are self-similarity adapted coordinates, is independent of initial field configuration. Note as an aside that we set $\Lambda = -\frac{\pi^2}{4}$ such that the boundary C is at $r = 1$. While this is convenient for visualisation, the solution can be extrapolated to other (non-zero) values of Λ by a rescaling of metric variables and scalar fields.

4.3.1 Critical regime and mass behaviour

We evolve ingoing Gaussian and kink curves and discuss the asymptotic mass behaviour $M(p)$. To locate the threshold value p^*, large numbers of simulations with different amplitudes are performed. Then the amplitude p^* is the field strength that separates field dispersal from black hole formation. Since only the initial strength of the field is important, one could in principle also change the width of the curve. Both leads to the same distinctive asymptotic mass behaviour [29]. We stress once again that the discussion in this chapter only refers to black hole formation before any reflection off the C boundary. Resolving AdS collapse after several reflections off the boundary is mathematically much more challenging. The pioneer work in this field [6] is reviewed in chapter 5.

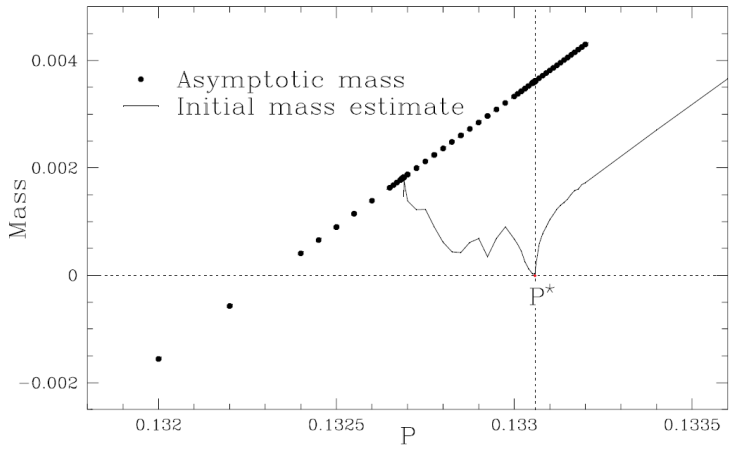

Fig. 4.3.1 Asymptotic mass (dots) and initial mass estimate (line) at the apparent horizon as a function of the initial amplitude p for a Gaussian curve ($n = 1$) where $\Lambda = -\frac{\pi^2}{4}$. The mass is only estimated in case of formation of an apparent horizon within simulation time. (taken from [29])[2]

[2] Since future figures in this chapter are taken from the same source [29], we only explicitly mention it once.

Figure 4.3.1 shows the asymptotic mass as a function of initial amplitude p. As a reference for future figures in this chapter, the Gaussian curve with $n = 1$ has width 0.05 and is centered around $r = 0.2$, the cosmological constant is $\Lambda = -\frac{\pi^2}{4}$. The amplitude is tuned from fairly subcritical to supercritical values. In case that an apparent horizon forms within the simulation time, the mass is estimated at the AH by equation 4.34. We are particularly interested in these values for slightly supercritical amplitudes. The strong increase above p^* supposes a universal scaling behaviour proportional to $(p - p^*)^{2\gamma}$.

In [29] the exponent $\gamma = 1.2 \pm 0.05$ is determined by the maximum Ricci curvature's scaling behaviour (c.f. section 4.3.2). The mass scaling discussion is slightly vague and conjectures that it roughly obeys the same scaling exponent. Thus, using their results, we checked that the slope in double log scale agrees with this numerical value of γ. However, the values only coincide over a short range very close to the threshold. The physical reason why the mass scaling is hard to observe lies in the reflecting boundary properties of AdS. Any outgoing components that do not collapse in first instance bounce off the boundary and falsify the measurement.

4.3.2 Universal phenomena and scaling exponent

To confirm universality, we begin by quoting (Z, T) coordinates that are well-adapted to self-similarity. In addition, a plot of the scale-invariant function $\phi_{,ZZ}(Z, T)$ reveals the wave nature of the critical solution. We then show that profiles of Gaussian, Gaussian-squared and kink initial data are locally indistinguishable in the critical limit. This section finishes with a determination of the scaling exponent γ, which is as expected independent of initial data.

To reveal the underlying continuous self-similarity, we introduce adapted coordinates. Numerical experimentation yields the (unique) scale-invariant variable [29]

$$x = \frac{\hat{r}}{t_c}, \quad \hat{r} = l \tan(r/l)\, e^B, \quad \text{where} \tag{4.35}$$

t_c is proper time measured by an observer along the $r = 0$ axis. The adapted coordinates are then expressed in log scale

$$Z \equiv \log(\hat{r}), \qquad T \equiv -\log(t_c). \tag{4.36}$$

The outcome of switching to (Z, T) variables becomes clear in figures 4.3.2 and 4.3.21 which show the second derivative of the field $\phi(Z, T)$ for the same nearly critical solution as before. Apart from revealing the solution's wave nature, the first figure already suggests a universal behaviour. This is confirmed in the second figure, which shows an enlargement of the critical regime. In this limit, profiles of Gaussian, Gaussian-squared and kink initial data are indistinguishable and thus confirm universality.

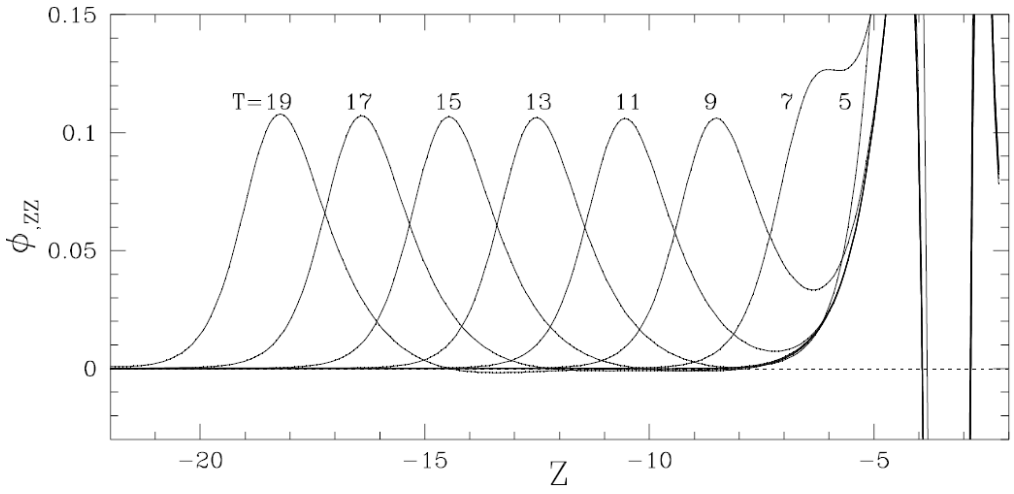

Fig. 4.3.2 The field's second derivative $\phi_{,ZZ}(Z,T)$ shows a universal wave behaviour. (initial data as before)

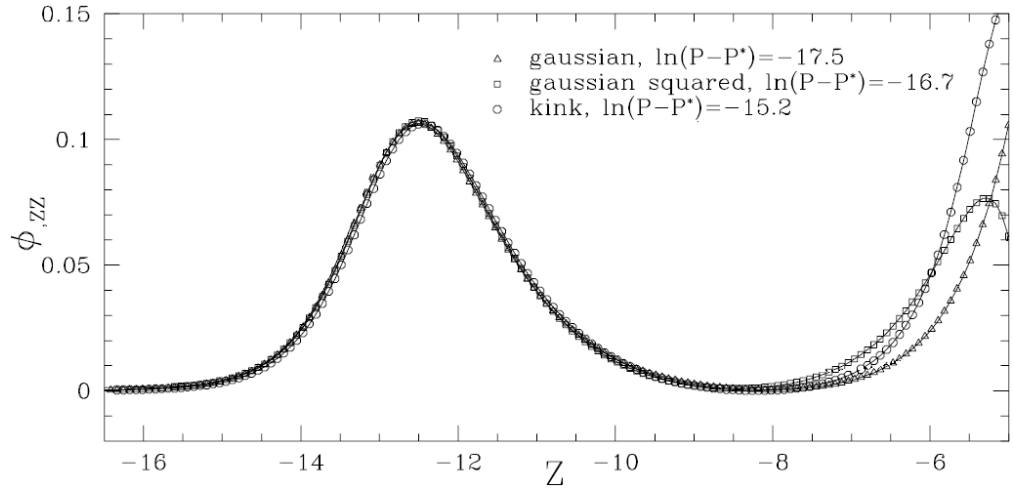

Fig. 4.3.21 Compares $\phi_{,ZZ}(Z,T)$ for marginally subcritical Gaussian, Gaussian-squared and kink initial data in the critical limit at $T = 13$. The profiles are indistinguishable.

Since the scaling behaviour of the mass estimate is hard to measure, the scaling exponent γ is determined by the maximum Ricci curvature scalar R_{max} in the critical regime. According to [20], we expect a behaviour of

$$R_{max} \propto (p^* - p)^{2\gamma} \,. \tag{4.37}$$

The factor of two occurs due to the quadratic length scale of curvature. Figure 4.3.22 shows a double *log* scale plot of R_{max} as a function of $(p^* - p)$. The linear regression functions for Gaussian

and kink initial data have slope $k_1 = -2.35$ and $k_2 = -2.48$. Even though the uncertainties are larger than in the non-AdS simulation (c.f. chapter 7), the results confirm a universal scaling behaviour with $\gamma = 1.2 \pm 0.05$. Since previous work focused on other types of matter, a comparison of the numerical value is not possible.

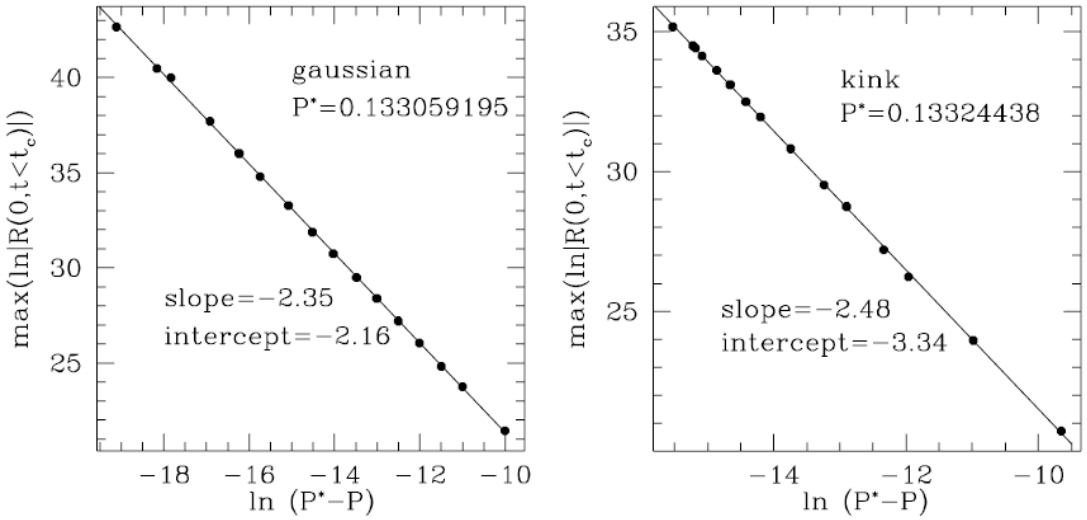

Fig. 4.3.22 Maximum Ricci curvature scalar R_{max} as a function of the aberration from the threshold in double log scale for nearly critical data. The least square method yields approximately coinciding slopes, which fix the value of the scaling exponent to $\gamma = 1.2 \pm 0.05$.

At the end of this chapter we remind us once again that peculiar geometric features of AdS make simulations more challenging. Even though the choice of coordinates and metric in [29] is tailored to particular needs of 2+1 dimensional AdS collapse, it is still difficult to observe e.g. mass scaling. Therefore, the scaling exponent is better determined by the maximum Ricci curvature scalar. The same approach is taken in chapter 7 where we solve the analogue non-AdS problem. In the context of universality we emphasise that transformation to self-similarity adapted coordinates (Z, T) revealed identical profiles in the critical regime for the field's second derivative for Gaussian, Gaussian-squared and kink initial data.

5 Weakly turbulent instability of AdS

While Minkowski and de Sitter space are stable under small perturbations, the maximally symmetric solution of Einstein's equations with negative cosmological constant is qualitatively different. Even though no-flux conditions on the timelike boundary ensure that anti-de Sitter space is *asymptotically* stable, local stability of AdS has until recently only been discussed in [2]. However a short time ago, Bizoń and Rostworowski took up this work and presented further results [6]. In fact they investigate the collapse in AdS similarly as in chapter 4, but with the difference of observing long-term field evolutions. Concretely, up to 10 reflections off the timelike boundary are resolved.

The second part of this paper entirely focuses on stability issues. We kept the structure similar to the original work due to rather complicated contents. Since an outline of the structure is found at the beginning of each section, we only state key results at this point. Bizoń and Rostworowski discover that the Ricci curvature scalar at the centre, a good indicator of stability, grows exponentially. Since the steady increase can not be cured by a rescaling of ϵ^{-2}, it is conjectured that anti-de Sitter space is unstable. By applying nonlinear perturbations to the solution, it turns out that *unremovable* resonant modes are responsible for this steady increase. Previous work on nonlinear wave equations on bounded domains [8, 14] suggests that this is connected with a shift of the energy spectrum towards high frequencies, which is indeed confirmed at the end of the chapter.

5.1 Metric and evolution equations

We solve the 4 dimensional Einstein equations with negative cosmological constant Λ for a real spherically symmetric massless scalar field

$$G_{\mu\nu} + \Lambda g_{\mu\nu} = 8\pi G\left(\partial_\mu\phi\partial_\nu\phi - \frac{1}{2}g_{\mu\nu}(\partial\phi)^2\right). \tag{5.1}$$

The scalar field equation is

$$g^{\mu\nu}\nabla_\mu\nabla_\nu\phi = 0. \tag{5.2}$$

The metric chosen in [6]

$$ds^2 = \frac{l^2}{\cos^2 x}\left(-Ae^{-2\delta}dt^2 + A^{-1}dx^2 + \sin^2 x\, d\Omega^2\right), \text{ where } l^2 = -\frac{3}{\Lambda}, \tag{5.3}$$

depends on the variables $A(t, x)$, $\delta(t, x)$ and $\phi(t, x)$. Its values for the pure AdS solution are $A(t, x) = 1$, $\delta(t, x) = 0$ and $\phi(t, x) = 0$. At the boundaries, smoothness and finiteness of the total mass give rise to a power series expansion of the metric variables. If we specify t to be proper time at the

centre, which implies $\delta(t,0) = 0$, then the expansion close to $x = 0$ depends on a single function $f_0(t)$:

$$\phi(t,x) = f_0(t) + O(x^2), \quad \delta(t,x) = O(x^2), \quad A(t,x) = 1 + O(x^2) \tag{5.4}$$

The approximation near $x = \frac{\pi}{2}$ is better expressed in terms of the auxiliary variable $\rho = \frac{\pi}{2} - x$ and is determined by two free functions $f_\infty(t)$ and $\delta_\infty(t)$ to

$$\phi(t,x) = f_\infty(t)\rho^3 + O(\rho^5), \quad \delta(t,x) = \delta_\infty(t) + O(\rho^6), \tag{5.5}$$

$$A(t,x) = 1 - 2M\rho^3 + O(\rho^6). \tag{5.6}$$

Since we consider the universal cover of AdS, the range of coordinates is $(-\infty < t < \infty, 0 \leq x < \frac{\pi}{2})$.

Defining auxiliary variables ($\Phi = \partial_x\phi, \Pi = A^{-1}\, e^{\delta}\, \partial_t\phi$) and substituting the metric 5.3 into the field equations, yields the wave equations

$$\partial_t\Phi = \partial_x(A\, e^{-\delta}\, \Pi), \quad \partial_t\Pi = \frac{1}{\tan^2 x}\partial_x(A\, e^{-\delta}\, \Phi \tan^2 x), \tag{5.7}$$

and constraint equations

$$\partial_x A = (1 - A)\, \frac{1 + 2\sin^2 x}{\sin x \cos x} - \sin x \cos x\; A(\Phi^2 + \Pi^2), \tag{5.8}$$

$$\partial_x \delta = -\sin x \cos x\, (\Phi^2 + \Pi^2), \tag{5.9}$$

$$\partial_t A + 2\sin x \cos x A^2\; e^{-\delta}\, \Phi\Pi = 0. \tag{5.10}$$

While equations 5.7-5.9 are solved with a 4^{th}-order finite-difference scheme, accuracy is monitored by the momentum constraint 5.10. Even though the problem is numerically challenging, Bizoń and Rostworowski do not reveal any details of their code. They only mention the use of the method of lines together with a 4^{th}-order Runge-Kutta scheme to solve 5.7. As usual, the metric variables are corrected in each step by the constraints 5.8 and 5.9.

5.2 Results

We consider solutions to Einstein's equations for Gaussian-like initial data

$$\Phi(0,x) = 0, \quad \Pi(0,x) = \frac{2\epsilon}{\pi} \exp\left(-\frac{4\tan^2 x}{\pi^2\sigma^2}\right), \text{ where } \sigma = \frac{1}{16}. \tag{5.11}$$

As in chapter 4, the field evolution collapses for amplitudes above a critical value ϵ_0. This is indicated by the formation of an apparent horizon at $x = x_H$, where the metric function $A(t,x)$ goes to zero. The horizon radius x_H then vanishes at the critical amplitude ϵ_0. So far nothing new, but in [6] the amplitude is now further decreased. Owing to the peculiar geometry of AdS, the wave packet with $\epsilon < \epsilon_0$ travels to and bounces off the timelike AdS boundary. Eventually, it collapses on

its way back to the centre. If the decrease of the amplitude is continued, a second critical amplitude ϵ_1 is found, where the horizon radius x_H again drops to zero. As shown in figure 5.2, continuously lowering the amplitude leads to a series of critical points ϵ_n. The subscript n counts the number of reflections off the boundary.

In principle the behaviour described above is not influenced by the cosmological constant. In other words the solution at ϵ_0 goes towards Choptuik's self-similar solution ($\Lambda = 0$). In particular the scaling behaviour of the horizon radius x_H in close proximity of each critical amplitude ϵ_n satisfies

$$x_H(\epsilon) \propto (\epsilon - \epsilon_n)^\gamma, \quad \gamma \approx 0.37. \tag{5.12}$$

The numerical value of the scaling exponent γ agrees with [9] and the result obtained in our simulation (c.f. section 7.4.4).

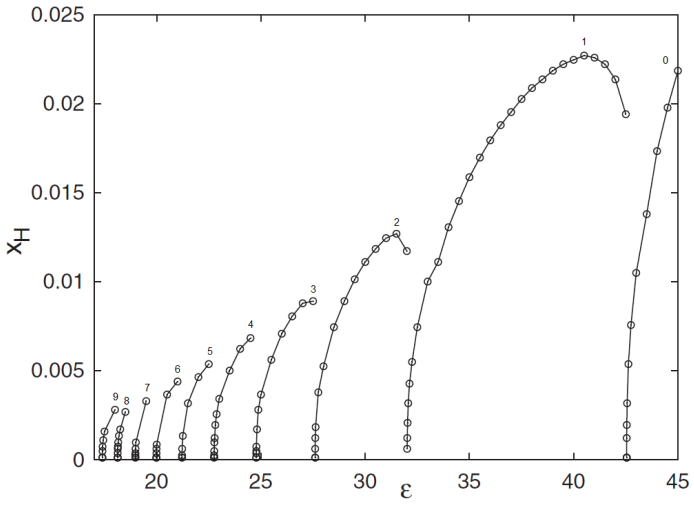

Fig. 5.2 Horizon radius x_H as a function of the amplitude ϵ of initial data 5.11. The number above each peak counts the reflections off the boundary before collapse. (taken from [6])[1]

In theory we expect an arbitrary number of critical amplitudes such that $\lim_{n\to\infty} \epsilon_n = 0$. This suggests the absence of a lower black hole threshold. In practice it is difficult to confirm this numerically, because computational cost significantly increases in long-term field observations. In fact it is remarkable that Bizoń and Rostworowski can resolve 10 reflections off the AdS boundary. Most other work as presented in chapter 4 almost entirely focuses on solutions *before* any reflection.

For completion of this section, we advert the reader to another critical behaviour illustrated in figure 5.2. Comparing the time in between *any* two neighbouring collapses, it turns out that the value $\Delta T \approx \pi$ is *universal*.

[1] Since future figures in this chapter are taken from the same source [6], we only explicitly mention it once.

5.2.1 Instability of AdS

This section focuses on results concerning instability of anti-de Sitter space. We begin by discussing the Ricci curvature scalar at $x = 0$, an indicator of instability, for weak Gaussian initial data. The observed exponential growth, which can not be cured by a rescaling of $\epsilon^{-2}R(\epsilon^2 t, 0)$, suggests that AdS space is unstable. Bizoń and Rostworowski apply weakly nonlinear perturbations to understand this feature. The solutions of the resultant differential equations give rise to *unremovable* resonant modes for higher-order initial data and thus confirm exponential instability. The conjecture in [6] is that these growing terms occur due to resonant mode mixing which focuses energy on higher frequencies only. This change of the energy spectrum is visualised at the end of the section.

The Ricci scalar at $x = 0$ is given by

$$R(t,0) = -\frac{2\Pi^2(t,0)}{l^2} - \frac{12}{l^2}. \tag{5.13}$$

The value of the curvature scalar oscillates, because the wave packet continuously travels in between the boundary and centre. Since we are interested in its instability behaviour, figure 5.2.1 depicts the upper envelope of the Ricci scalar. Even though initial amplitudes are weak, the curvature strongly increases after a constant phase at the beginning. Eventually, all solutions collapse after sufficiently large numbers (500 for lowest, 50 for highest amplitude) of reflections.

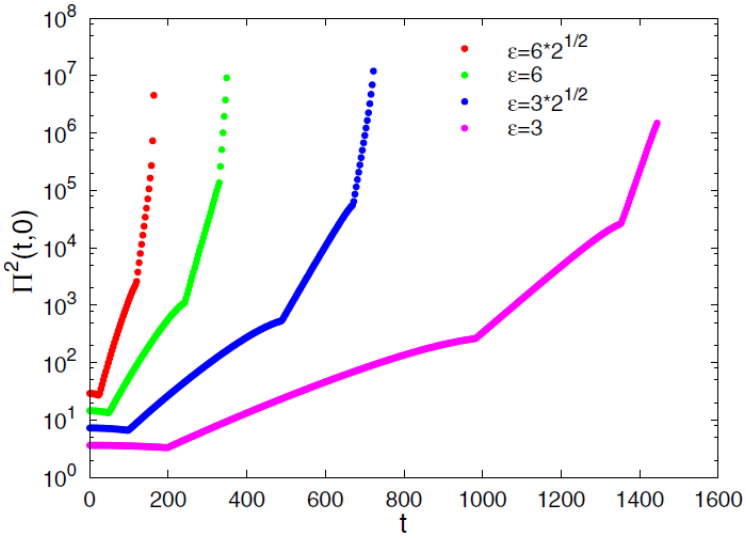

Fig. 5.2.1 Upper envelope of $\Pi^2(t,0)$ for weak initial data 5.11.

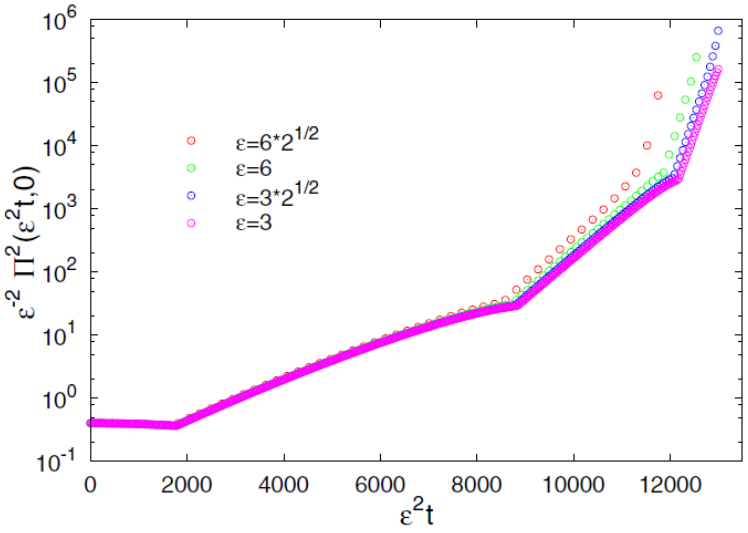

Fig. 5.2.11 Rescaled version of figure 5.2.1.

Figure 5.2.11 again shows the upper envelope of the curvature scalar for the same initial data. However, the data is rescaled by $\epsilon^{-2}R(\epsilon^2 t, 0)$. Since the rescaling does not remove steeper and steeper growth, infinitesimally small perturbations result in a steady increase. This is an indication of instability of AdS, which is best analysed by applying weakly nonlinear perturbations.

Nonlinear perturbations

In order to approximately solve equations 5.7-5.9 for weak initial data $(\phi, \partial_t\phi)_{t=0} = (\epsilon f(x), \epsilon g(x))$, we perturb the metric variables to [6]

$$A = 1 - \sum_{j=1}^{\infty} A_{2j}\epsilon^{2j},\ \delta = \sum_{j=1}^{\infty} \delta_{2j}\epsilon^{2j},\ \phi = \sum_{j=0}^{\infty} \phi_{2j+1}\epsilon^{2j+1},\ \text{where} \tag{5.14}$$

all but the first mode $(\phi_1, \partial_t\phi_1)_{t=0} = (f(x), g(x))$ are set to zero. Substituting this ansatz into the field equations leads to a differential equation at each order. We find at lowest order

$$\partial_t^2\phi_1 + L\phi_1 = 0, \quad L = -\frac{1}{\tan^2 x}\partial_x(\tan^2 x\,\partial_x). \tag{5.15}$$

The self-adjoint Sturm-Liouville operator on $L^2([0, \frac{\pi}{2}], \tan^2 x\,\mathrm{d}x)$ gives rise to the inner product $(f, g) := \int_0^{\pi/2} f(x)g(x)\tan^2 x\ \mathrm{d}x$ on this Hilbert space. The normalised eigenfunctions of the operator are

$$e_j(x) = \sqrt{\frac{16(j+1)(j+2)}{\pi}}\cos^3 x\ F_1(-j, j+3, \frac{3}{2}; \sin^2 x). \tag{5.16}$$

The associated *non-negative* eigenvalues ($\omega_j^2 = (3+2j)^2,\ j \geq 0$) ensure that AdS is stable at first order.

However, the solution at third order is qualitatively different. The projection of the inhomogeneous ODE

$$\partial_t^2\phi_3 + L\phi_3 = S(\phi_1, A_2, \delta_2) := -2(A_2+\delta_2)\partial_t^2\phi_1 - (\partial_t A_2 + \partial_t\delta_2)\partial_t\phi_1 - (\partial_x A_2 + \partial_x\delta_2)\partial_x\phi_1 \quad (5.17)$$

onto the e_j basis of the Sturm-Liouville operator leads to an infinite number of harmonic oscillators

$$\partial_t^2 c_j + \omega_j^2 c_j = S_j := (S, e_j). \quad (5.18)$$

A lengthy calculation [6] then shows that a set of three indices j_i, whose linear solution modes of equation 5.15 are non-vanishing and whose eigenvalues satisfy $\omega_j = \omega_{j_1} + \omega_{j_2} - \omega_{j_3}$, are a *resonant* solution of 5.18. Thus, arbitrarily small perturbations result in steeper and steeper growth, which indicates that anti-de Sitter space is unstable. While resonant terms can be removed for one-mode data, higher-order initial data leads to a growing number of *unremovable* secular terms.

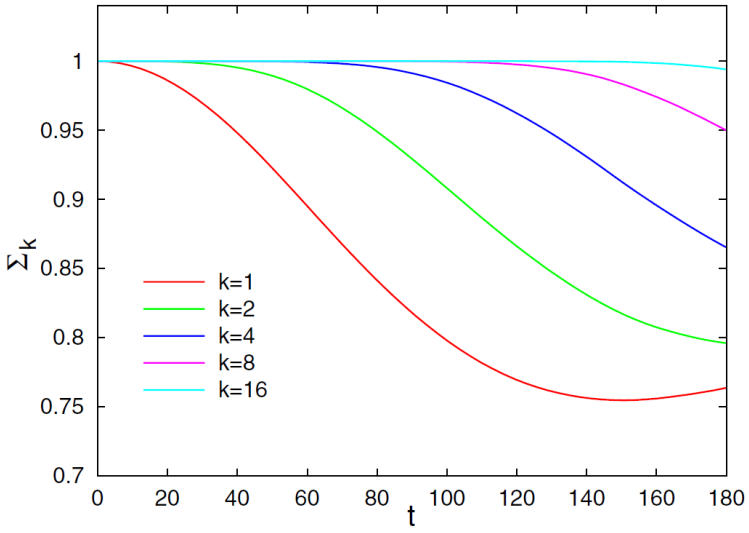

Fig. 5.2.12 Fraction of the total energy incorporated in the first $(k+1)$ modes $\Sigma_k := \frac{1}{M}\sum_{j=0}^{k} E_j$ for two-mode initial data 5.21.

Previous work on related problems, e.g. the nonlinear Schrödinger equation on a torus [8, 14], suggests that this instability is connected with a shift of energy towards higher frequencies. In fact this feature actually occurs and is visualised by measuring the fraction of the total energy contained in the first $(k+1)$ modes. The energy of the j^{th} mode, where $\Phi_j := (\sqrt{A}\Phi, e_j')$ and $\Pi_j := (\sqrt{A}\Pi, e_j)$ are projections of the auxiliary variables, is

$$E_j(t) = \Pi_j^2 + \omega_j^{-2}\Phi_j^2. \quad (5.19)$$

The total energy is then given by

$$M = \frac{1}{2}\int_0^{\pi/2} (A\Phi^2 + A\Pi^2)\tan^2 x \, \mathrm{d}x = \sum_{j=0}^{\infty} E_j(t) := \sum_{j=0}^{\infty} \Pi_j^2 + \omega_j^{-2}\Phi_j^2. \tag{5.20}$$

The results in figure 5.2.12 confirm this shift of energy for initial data

$$\phi(0, x) = \epsilon\left(\frac{1}{d_0}e_0(x) + \frac{1}{d_1}e_1(x)\right) \text{ with } \epsilon = 0.088. \tag{5.21}$$

6 A summary for elementary numerical methods

Since it is hard to solve Einstein's field equations analytically, numerical methods are widely used in general relativity. While in special relativity the evolution of a scalar field is exactly known, the analogous problem including matter-geometry coupling is better solved numerically. In this chapter we therefore briefly review numerical integration and differentiation based on [27]. In addition the Euler method, a first-order scheme for integrating ordinary differential equations, is introduced. Since Einstein's equations are reformulated as an ODE system in chapter 7, we waive a discussion of partial differential equations and refer to [3] for a review in the context of general relativity.

6.1 Numerical integration

A one-dimensional definite integral $\int_a^b f(x)\,\mathrm{d}x$ is usually solved by finding the antiderivative $F(x)$. Then the fundamental theorem of calculus yields $\int_a^b f(x)\,\mathrm{d}x = F(b) - F(a)$. However, if the antiderivative is either not an elementary function or if the values of the function $f(x)$ are only known at specific points, then the integral has to be solved numerically.

Quadrature rules

Numerical integration *locally* approximates an integral by a weighted sum of function values at s *integration points* c_i

$$\int_0^1 f(x)\,\mathrm{d}x \approx \sum_{i=1}^{s} b_i f(c_i). \tag{6.1}$$

Since smooth well-behaved functions can be Taylor-expanded, a quadrature rule should lead to an accurate integration result for a polynomial of sufficiently high order while only requiring few integration points. The idea of the value of a definite integral being the area below the graph of the function $f(x)$ suggests to approximate the integral by the area of a trapezoid. This is achieved by choosing the integration points $c_1 = 0, c_2 = 1$ and the weights $b_1 = \frac{1}{2}, b_2 = \frac{1}{2}$. This quadrature formula is referred to as trapezoid rule and accurately integrates polynomials up to order one. It turns out that we can do much better.

The most efficient quadrature rules are *Gaussian quadrature* rules. A Gaussian quadrature rule with s integration points, whose values are given by the zeros of the Legendre polynomial

P_s, accurately integrates polynomials up to order $p = 2s - 1$. A sample code of the Gaussian quadrature rule of order 5 for MATLAB is found in Annex. The integration points are $c_1 = \frac{1}{2} - \frac{\sqrt{15}}{10}, c_2 = \frac{1}{2}, c_3 = \frac{1}{2} + \frac{\sqrt{15}}{10}$, the weights are given by $b_1 = \frac{5}{18}, b_2 = \frac{8}{18}, b_3 = \frac{5}{18}$.

To numerically integrate $\int_a^b f(x)\,\mathrm{d}x$, we divide the integration interval $[a, b]$ into N subintervals (bounded by x_j, x_{j+1}), transform the overall limit to $[0, 1]$ and apply equation 6.1. Transforming back to the initial interval yields

$$\int_a^b f(x)\,\mathrm{d}x = \sum_{j=0}^{N-1} \int_{x_j}^{x_{j+1}} f(x)\,\mathrm{d}x \approx \sum_{j=0}^{N-1} h_j \sum_{i=1}^{s} b_i f(x_j + c_i h_j), \tag{6.2}$$

where h_j denotes the length of each subinterval.

6.1.1 Adaptive stepsize control

In practice we often require accurate results up to a tolerance TOL. Apart from using suitable quadrature rules, the choice of subintervals in equation 6.2 is crucial. Intuitively, whenever the function $f(x)$ changes considerably, the stepsize h has to be reduced to maintain accuracy. A way to implement this is as follows.

For each subinterval, we compute the value of the integral and its error using a quadrature rule. If the sum of the errors is larger than the tolerance, the subinterval with the biggest error is divided into two halves. This process is repeated until a required accuracy is achieved. A possibility to code this procedure in MATLAB is by storing the data of each subinterval in a row of a matrix. The endpoints are saved in the first two columns; the last two columns correspond to the values of the integral and the error. While $|error| > TOL$, we apply the command *sortrows* to determine the subinterval of largest error and then divide it into two halves. Since error estimates are not needed in this dissertation, it is sufficient to name *Richardson extrapolation* and *embedding of quadrature rules* as common techniques for one-dimensional integration. Further discussion including source codes for C and FORTRAN is found in [28].

6.2 Numerical differentiation

As with numerical integration, the main application of numerical differentiation is the computation of the derivative of a function whose values are only numerically known. Formulas for numerical approximations of derivatives are derived by Taylor-expanding

$$f(x + h) = f(x) + hf'(x) + \frac{h^2}{2} f''(\xi), \qquad x < \xi < x + h. \tag{6.3}$$

Rearranging leads to

$$f'(x) = \frac{f(x + h) - f(x)}{h} - \frac{h}{2} f''(\xi). \tag{6.4}$$

The term proportional to h is the error of approximation. Together with the round-off error, which is proportional to machine epsilon over h, the ideal choice of h is if the two errors are equal (c.f. figure 6.2).

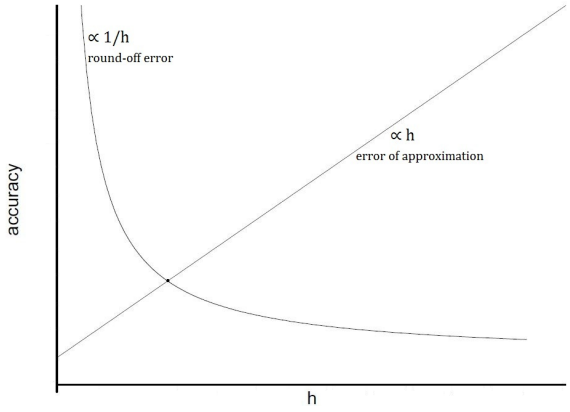

Fig. 6.2 Stepsize dependence of the accuracy of the first-order derivative approximation.

Taylor-expanding $f(x + h)$ and $f(x - h)$ yields the second-order approximation

$$f'(x) = \frac{f(x+h) - f(x-h)}{2h} - \frac{h^2}{6} f'''(\xi). \tag{6.5}$$

Formulas for higher-order derivatives are determined analogously. In addition, these ideas extend to functions of two variables by separately *finite differencing* in the direction of each variable.

6.3 Numerical ordinary differential equations

Numerical schemes for ordinary differential equations are required if analytic solutions do not exist. The intuitive approach is as follows. Starting from a given initial value at time $t = 0$, we extrapolate to later times by the rate of change. As the rate of change is time-dependent, the interval has to be divided into sufficiently small subintervals. We derive the simplest explicit first-order method for solving ODE's which is referred to as Euler method. Small modifications lead to the implicit second-order Crank-Nicolson scheme.

6.3.1 Euler method

Since we are looking for an approximate solution to the initial value problem

$$y'(x) = f(x, y(x)), \quad y(x_0) = y_0, \tag{6.6}$$

the interval $[x_0, x_{max}]$ is divided into subintervals of length h. One way to derive the Euler method is to integrate equation 6.6

$$y(x_0 + h) - y(x_0) = \int_{x_0}^{x_0+h} f(x, y(x))\,\mathrm{d}x \approx hf(x_0, y(x_0)), \tag{6.7}$$

and to approximate by the left-hand rectangle quadrature rule ($c_1 = 1, c_2 = 0$). Rearranging leads to the Euler method

$$y(x_{n+1}) = y(x_n) + hf(x_n, y_n), \quad x_n = x_0 + nh. \tag{6.8}$$

Even though the Euler scheme is simple in derivation and implementation, poor accuracy and stability problems often demand for more sophisticated methods.

6.3.2 Crank-Nicolson method

The Crank-Nicolson method is an implicit second-order finite difference method which combines the forward- and backward Euler method. The forward Euler scheme is the one considered so far, the backward one is obtained by using the right-hand rectangle quadrature rule ($c_1 = 0, c_2 = 1$) in equation 6.7:

$$y(x_{n+1}) = y(x_n) + hf(x_{n+1}, y_{n+1}) \tag{6.9}$$

Combining equations 6.8 and 6.9 yields the Crank-Nicolson method

$$y(x_{n+1}) = y(x_n) + \frac{h}{2}\Big(f(x_n, y_n) + f(x_{n+1}, y_{n+1})\Big). \tag{6.10}$$

The difficulty with equation 6.10 is that y_{n+1} occurs on both sides. One approach is to *predict* y_{n+1} on the right-hand side using the forward Euler method and to *correct* the value with equation 6.10.

7 Spherically symmetric collapse code for a massless scalar field

The collapse of a massless self-gravitating scalar field has amongst others earlier been discussed by Choptuik [9, 10], Christodoulou [12, 13] and Garfinkle [15]. Their work mainly focused on solutions close to the black hole threshold separating black hole formation from field dispersal and concluded that in this critical limit the field evolution at late times obeys a "ringing" solution independent of initial data. If black holes form, the mass satisfies a power law $m_{BH} = K(p - p^*)^\gamma$ with γ fixed and K being a constant dependent on the black hole family. Both results also agree with the theoretical prediction of critical phenomena (c.f. chapter 2). In addition, it is shown that curvature scalar and field energy density increase unconfined near the axis, which can even be seen by distant observers.

In this chapter we simulate the spherically symmetric collapse of a massless scalar field in flat space based on an algorithm suggested by Hamadé and Stewart [21]. We extend their code to include a cosmological constant and this is the first time the problem is solved using double null coordinates. By introducing a set of auxiliary variables, Einstein's field equations are formulated as a first-order system, which is solved with both the Euler and a second-order predictor-corrector method. We reproduce Hamadé's and Stewart's results of the scalar field, the metric function and the Ricci curvature scalar on the $r = 0$ axis. In the context of universality it is further confirmed that the maximum Ricci curvature scalar and the black hole mass obey a power law with an exponent independent of the cosmological constant and the black hole family.

7.1 Line element and coordinates

We solve Einstein's field equations

$$G_{\mu\nu} + \Lambda g_{\mu\nu} = R_{\mu\nu} - \frac{1}{2}Rg_{\mu\nu} + \Lambda g_{\mu\nu} = 8\pi G T_{\mu\nu} \tag{7.1}$$

for a real spherically symmetric massless scalar field. The energy-momentum tensor is

$$T_{\mu\nu} = \psi_{,\mu}\psi_{,\nu} - \frac{1}{2}g_{\mu\nu}g^{\alpha\beta}\psi_{,\alpha}\psi_{,\beta}\,. \tag{7.2}$$

Energy conservation or the contracted Bianchi identities yield the scalar field equation

$$\Box\psi = 0. \tag{7.3}$$

First numerical results were published by Choptuik who suggested using time t and physical area radius r coordinates with the line element

$$ds^2 = -\alpha^2(t,r)dt^2 + a^2(t,r)dr^2 + r^2 d\Omega^2, \tag{7.4}$$

where $d\Omega^2$ is the usual round two-sphere metric $\mathcal{S}^2$ in polar coordinates (θ, ϕ). This line element breaks down at an apparent horizon and is therefore not suitable for studying strong-field regions. Garfinkle [15] proposed null coordinates to solve this issue. While a line element with one null coordinate is unstable for critical field configurations, double null coordinates (u, v) maintain stability and do not break down:

$$ds^2 = -a^2(u,v)dudv + r^2(u,v)d\Omega^2. \tag{7.5}$$

The related spherically symmetric spacetime manifold is $\mathcal{M} = \mathcal{N}\times\mathcal{S}^2$ where $\mathcal{N}$ is a two-dimensional Riemannian manifold. Since each point of $\mathcal{N}$ lies on either a past or future null cone, (u, v) and (u, θ, ϕ, v) provide coordinate charts on $\mathcal{N}$ and $\mathcal{M}$. The scalar field equation 7.3 in this chart is

$$r\psi_{uv} + r_u\psi_v + r_v\psi_u = 0. \tag{7.6}$$

To rewrite Einstein's equations in terms of the coordinates (u, θ, ϕ, v), we compute the Riemann and Ricci tensor by using the values of the non-vanishing Christoffel symbols Γ^u_{uu}, $\Gamma^u_{\theta\theta}$, $\Gamma^u_{\phi\phi}$, $\Gamma^\theta_{u\theta}$, $\Gamma^\theta_{\phi\phi}$, $\Gamma^\theta_{\theta v}$, $\Gamma^\phi_{u\phi}$, $\Gamma^\phi_{v\phi}$, $\Gamma^\phi_{\theta\phi}$, $\Gamma^v_{\theta\theta}$, $\Gamma^v_{\phi\phi}$, Γ^v_{vv}. These yield the components of the Einstein tensor (subscripts on the right side abbreviate derivatives):

$$G_{uv} = r^{-2}\left(\frac{1}{2}a^2 + 2r_u r_v + 2rr_{uv}\right), \tag{7.7}$$

$$G_{uu} = 2r^{-1}\left(\frac{2r_u a_u}{a} - r_{uu}\right), \tag{7.8}$$

$$G_{vv} = 2r^{-1}\left(\frac{2r_v a_v}{a} - r_{vv}\right), \tag{7.9}$$

$$G_{\phi\phi} = \sin(\theta)^2 G_{\theta\theta} = \sin(\theta)^2\left(2r^2a^{-2}\left(\frac{a_u a_v}{a} - a_{uv}\right) - \frac{4rr_{uv}}{a}\right), \tag{7.10}$$

the corresponding Einstein equations are

$$rr_{uv} + r_u r_v + \frac{1}{4}\left(1 - \Lambda r^2\right)a^2 = 0, \tag{7.11}$$

$$r_{uu} - 2a^{-1}r_u a_u + 4\pi G r\psi_u^2 = 0, \tag{7.12}$$

$$r_{vv} - 2a^{-1}r_v a_v + 4\pi G r\psi_v^2 = 0, \tag{7.13}$$

$$a^{-1}a_{uv} - a^{-2}a_u a_v + r^{-1}r_{uv} + 4\pi G\psi_u\psi_v - \frac{1}{4}\Lambda a^2 = 0. \tag{7.14}$$

These equations are not independent and thus evaluating a subset is sufficient. However, it is hard to achieve numerical stability for equation 7.14, which must not be omitted. From this point on there are different ways to proceed. We follow the idea in [21] and introduce various auxiliary variables in order to rewrite the equations above as a first-order differential system. Even though the problem expands to a high number of equations, the proposed algorithm is conceptually simple and numerically stable. Both will be discussed in the next two sections.

7.2 Auxiliary variables and equations, physical quantities

We introduce auxiliary variables

$$c = \frac{a_u}{a}, \quad d = \frac{a_v}{a}, \quad f = r_u, \quad g = r_v, \quad s = \sqrt{4\pi G}\psi, \quad p = s_u, \quad q = s_v. \tag{7.15}$$

Important physical quantities in terms of these variables are the Ricci curvature

$$R(u,v) = -\frac{8pq}{a^2}, \tag{7.16}$$

the scalar field's energy density

$$\rho(u,v) = \frac{1}{8\pi G a^2}(p^2 + q^2), \tag{7.17}$$

and for strong fields the Hawking mass

$$m(u,v) = \frac{r}{2}\left(1 + \frac{4fg}{a^2}\right). \tag{7.18}$$

To visualise the evolution of the scalar field, the metric function and the Ricci curvature on the $r = 0$ axis, we require the proper time T experienced by an observer moving along it

$$T(u,u)|_{r=0} = \int_0^u a(x,x)\,\mathrm{d}x. \tag{7.19}$$

The scalar and Einstein field equations expand into a first-order differential system of 14 equations. Since some are dependent, only these 8 equations are relevant for the algorithm we use:

$$\begin{aligned}
F1: &\quad q_u = -\frac{fq+gp}{r},\\
F2: &\quad d_u = \frac{fg+\frac{1}{4}a^2}{r^2} - pq,\\
F3: &\quad a_v = ad,\\
F4: &\quad r_v = g,\\
F5: &\quad s_v = q,\\
F6: &\quad p_v = -\frac{fq+gp}{r},\\
F7: &\quad f_v = -\frac{fg+\frac{1}{4}a^2}{r} + \frac{1}{4}\Lambda r a^2,\\
F8: &\quad g_v = 2dg - rq^2.
\end{aligned} \tag{7.20}$$

It is to note that equations $F1$ and $F2$ evolve in u-direction, whereas the remainder formulas contain only v-derivatives. Particular care is needed with equations $F1$, $F2$, $F6$ and $F7$ since these diverge on the $r = 0$ axis.

7.2.1 Initial and boundary data

We want to solve the system 7.20 on the (u, v)-grid bounded by the $u = v$ (or $r = 0$) axis. The algorithm in section 7.3 requires both initial and boundary data. Since the geometry is flat on the initial null cone $C_+(u = 0, v)$, we have $d(0, v) = 0$. In other words the geometry on the initial slice is set independently of the cosmological constant Λ. The shape of the ingoing scalar field specifies $s(0, v)$ from which its gradient $q|_{(0,v)} = s_v|_{(0,v)}$ is computed. In addition, we need boundary values for the variables a, s, f, g and p. While a and s boundary data are harder to compute, equations 7.20 immediately yield $g = -f = \frac{1}{2}a$ and $p = q$ for $r = 0$.

The remaining variables on the axis, i.e. values for the scalar field s and the metric function a, are determined by the condition

$$\frac{\partial s}{r} = \frac{\partial a}{r} = 0. \tag{7.21}$$

The predictor-corrector method requires a second-order approximation of 7.21 linking s at $r = 0$, dr and $2dr$. Since the algorithm starts on the null cone $C_+(0, v)$, $s(2dr)$ and $s(dr)$ are computed first and then used to determine $s(0)$. The required formula is derived by imposing 7.21 and $s(0) = s_0$, $s(dr) = s_1$, $s(2dr) = s_2$ on an arbitrary second-order polynomial. This leads to a system of two equations which is solved for s_0

$$s_0 = \frac{1}{3}(4s_1 - s_2). \tag{7.22}$$

The metric function a is treated similarly. While all the required data are now assembled, this might not be clear until we reveal in the next section how the algorithm moves through the (u, v)-grid.

7.3 Algorithm: second-order predictor-corrector method

The structure of 7.20 suggests to separately evolve in u- ($F1$ and $F2$) and v-direction (remaining equations). In compact notation, 7.20 is rewritten as

$$y_u = F(y, z),\ z_v = G(y, z), \quad \text{where } y = \{q, d\}\,,\ z = \{a, r, s, p, f, g\}\,. \tag{7.23}$$

The algorithm proposed in [21] computes values at each point $n = (u, v)$ in terms of values at $e = (u - h, v)$ and $w = (u, v - h)$. To assure stability, a second-order predictor-corrector method (c.f. section 6.3.2) is used. In the predictor step y- and z-values are explicitly computed by

$$\hat{y}_n = y_e + hF(y_e, z_e), \tag{7.24}$$

and

$$\hat{z}_n = z_w + \frac{1}{2}h\left(G(y_w, z_w) + G(\hat{y}_n, \hat{z}_n)\right). \tag{7.25}$$

Even though it is not obvious, the implicit equation 7.25 can be rearranged into an explicit form. In the corrector step these values are corrected by

$$y_n = \frac{1}{2}\left(y_e + \hat{y}_n + hF(\hat{y}_n, \hat{z}_n)\right), \tag{7.26}$$

and

$$z_n = \frac{1}{2}\left(z_w + \hat{z}_n + hG(\hat{y}_n, \hat{z}_n)\right). \tag{7.27}$$

The method presented above suggests to move through the (u, v)-grid along a set of null cones $C_+(u = nh, v)$. While $F1$ and $F2$ predict the (q, d)-values onto each future null cone, radial integrations from $v = 0$ to v_{max} using the remaining equations complete the solution.

We have implemented the algorithm above and a second version using a first-order explicit Euler method in MATLAB. Both codes simulate the spherically symmetric collapse of a massless scalar field. While the predictor-corrector scheme should lead to better stability properties, our code occasionally fails in regions close to the $r = 0$ axis. It is too sensitive to the choice of initial data, number of grid-points and stepsize to work with it in practice. Due to the high number and complexity of the equations, it is difficult to judge why the code fails. Anyway, for non-critical data the results of the two versions agree with each other. A consequence of using the first-order code is that less oscillations of the fields (c.f. section 7.4) are resolved before the computer runs out of memory.

However, for the purposes we require, the first-order code works well enough. In addition, precise results for highly-critical initial data require much more effort. While our code uses a uniform grid, Hamadé and Stewart work with adaptive mesh refinement based on [5]. Even though a simplified version for a spherically symmetric collapse was found, it is still too difficult to include it in this dissertation. However, the fundamental idea is the same as for one-dimensional integration (c.f. section 6.1.1). To obtain accurate data, the grid is refined in regions where the variables change much. In regions of less activity, the grid remains coarse.

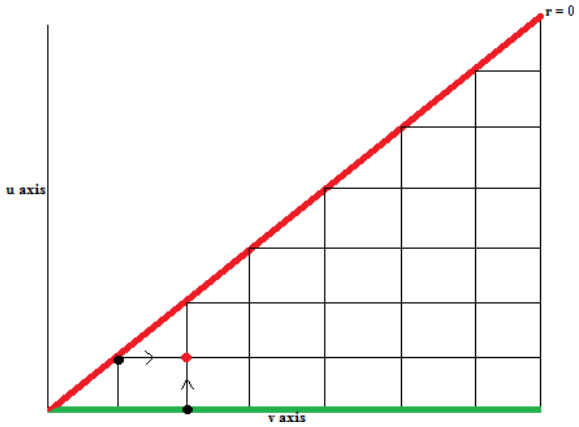

Fig. 7.3 A sketch of the (u, v)-grid. Initial data of d, q and s are specified on the null cone $C_+(u = 0, v)$ (green), boundary values of a, s, f, g and p are required along the $r = 0$ axis (red). The algorithm moves through the grid from the bottom-left to the top-right as indicated by arrows.

In the next section the collapse is simulated with 3 different MATLAB codes (c.f. Annex). While the idea of our codes is described in section 7.3, Toby Wiseman's sample code *collapsenull* (as presented in the QFFF special topic lectures) uses non-linear recursion to solve the problem. Even though the results agree with each other, resolution and computational cost differ significantly. Computations with the non-linear recursion version take much longer and yield only a coarse resolution. However, we could resolve 4 field oscillations on axis. The first-order code shows less peaks due to the missing mesh-refinement (c.f. section 7.4), but with high resolution. In addition, it allows a non-zero cosmological constant Λ in Einstein's equations.

7.4 Results

We begin the discussion of the results of the simulation of the spherically symmetric collapse of a massless scalar field by pointing out the differences in the evolution of a scalar field with and without matter-geometry coupling. Then the scalar field, the metric function and the Ricci curvature scalar are plotted on axis. We also argue why the unconfined increase of the curvature scalar and the field energy density near the axis is seen by a distant observer. The final subsection focuses on universal phenomena. We confirm that both the maximum Ricci curvature scalar and the black hole mass follow a power law with an exponent independent of the black hole family.

7.4.1 Influence of matter-geometry coupling

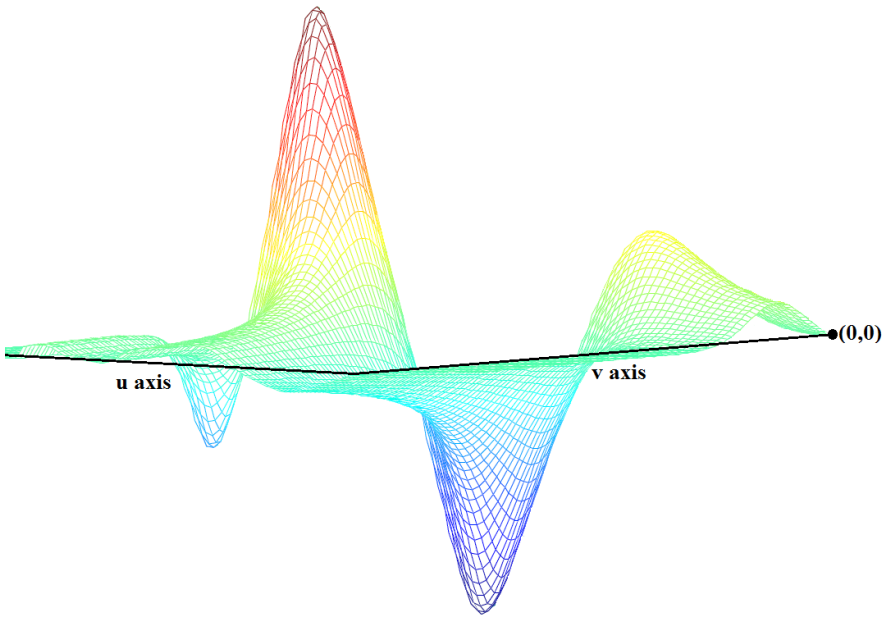

Fig. 7.4.1 Evolution of a marginally subcritical scalar field *including* matter-geometry coupling ($\Lambda = 0$).

Evolving a scalar field in Minkowski spacetime is achieved by solving the non-linear wave equation. In double null coordinates ($u = t - r$, $v = t + r$) the initial pulse specified on $C_+(u = 0, v)$ travels towards the $r = 0$ axis, bounces off and leaves to future null infinity. The shape of each pulse depends on initial data. The late field configuration is flat. In the case of matter-geometry coupling, the scalar field either disperses ($p < p^*$) or forms a black hole ($p > p^*$). P^* is referred to as *critical parameter* and defined as the value separating those two events. Its value is determined by a sequence of simulations around the threshold of black hole formation. While a solution of a finally dispersing field is clearly subcritical, the formation of an apparent horizon and of a singularity in the supercritical case makes it more difficult to visualise these solutions. It turns out that if matter geometry-coupling is switched on, the evolution heavily depends on the choice of initial data. In case of a weak field on the $C_+(u = 0, v)$ cone, the effects of the coupling are negligible and we find a similar behaviour as before.

Figure 7.4.1 depicts the evolution of a *marginally subcritical* Gaussian scalar field. It moves from past (right) to future (left) timelike infinity. The incoming Gaussian function reflects off the $r = 0$ axis (background boundary) and continues towards future null infinity. Due to matter-geometry coupling, we see another peak on the axis, with a third one just building up. At late times the scalar field is not zero, but we expect a "ringing" solution independent (universal) of the ingoing pulse.

7.4.2 Scalar field, metric function and Ricci curvature on axis

By plotting the scalar field s on the $r = 0$ axis, we find that the smaller $p^* - p$ gets, the more peaks build up. This proposes that an arbitrary number of oscillations is seen for sufficiently small deviations from the threshold. Since the *exactly* critical case will never be achieved in numerical simulations, no proof for this statement has been found yet. Thus, an alternative approach for discussing *late* time evolution right on the threshold would be some nice future work. Anyway, in [21] up to 5 peaks are resolved on axis. The code *collapsenull* computes 4 oscillations after specifying 14 (sic!) digits beyond the decimal point. However, the resolution is low. Figure 7.4.2 shows two field oscillations on axis for the same *marginally subcritical* Gaussian initial data as in figure 7.4.1. The *universal* time between the peaks is $\Delta\tau \approx 1.46$ and roughly agrees with the value $\Delta\tau \approx 1.49$ in [21]. As mentioned before, more difficult codes are required for precise results in proximity of the black hole threshold.

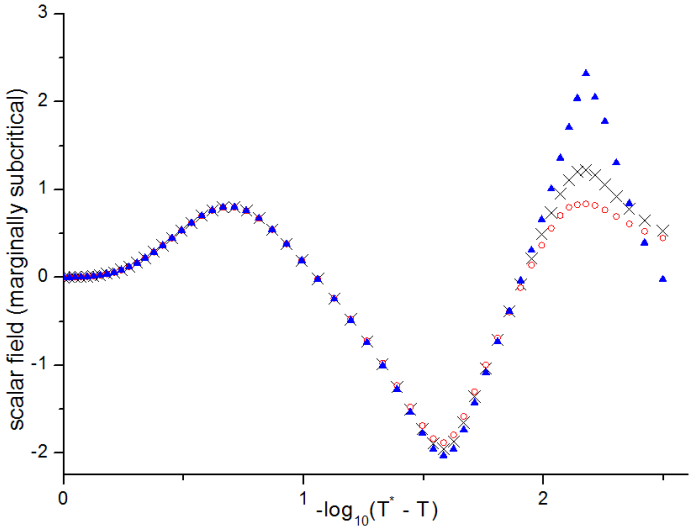

Fig. 7.4.2 Scalar field s (with fixed amplitude p) on axis in terms of $\tau = -\log_{10}(T^* - T)$ for $\Lambda = 0$ (black crosses), $\Lambda = 100$ (red circles) and $\Lambda = -100$ (blue triangles) where T^* is critical time.

To interpret the influence of the cosmological constant Λ, we recap that it only occurs in equation F7

$$f_v = -\frac{fg + \frac{1}{4}a^2}{r} + \frac{1}{4}\Lambda r a^2, \quad \text{where } f = r_u. \tag{7.28}$$

A large positive Λ (expanding) implies a rapid change of r along the (u, v)-grid and increases the threshold value p^*. Since we do not adjust p, the solution with a positive cosmological constant (c.f. figure 7.4.2, red circles) is subcritical and therefore has less oscillations. A negative Λ corresponds to an attractive geometry and supports the gravitational collapse such that the evolution breaks down earlier. Since p is very close to the critical parameter p^* for $\Lambda = -100$, the amplitude of the

second peak (blue triangles) is significantly larger. However, if the cosmological constant is further decreased, the field collapses. In addition it is worth of note that, as expected due to universality, the time in between the field oscillations is not affected by the cosmological constant.

Other important physical quantities are the metric function and the Ricci curvature. In figure 7.4.21 the metric function a is plotted on axis as a function of τ for the same initial data. Since a is quadratic in the derivatives of the scalar field s, we see the double number of oscillations. The more critical the initial data, the faster a drops. The metric function a goes towards zero at the singularity.

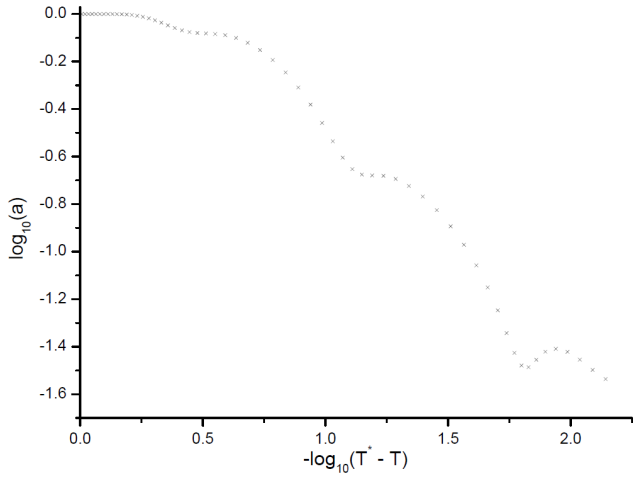

Fig. 7.4.21 Metric function a on axis in terms of $\tau = -\log_{10}(T^* - T)$ for $\Lambda = 0$.

Its values are not only used to compute the proper time T of an observer on the axis

$$T(u,u)|_{r=0} = \int_0^u a(x,x)\,\mathrm{d}x, \tag{7.29}$$

but the metric function a also occurs in the denominator of the Ricci scalar

$$R(u,u) = -\frac{8p^2}{a^2} = -32\pi G\frac{d^2\psi}{dT^2}. \tag{7.30}$$

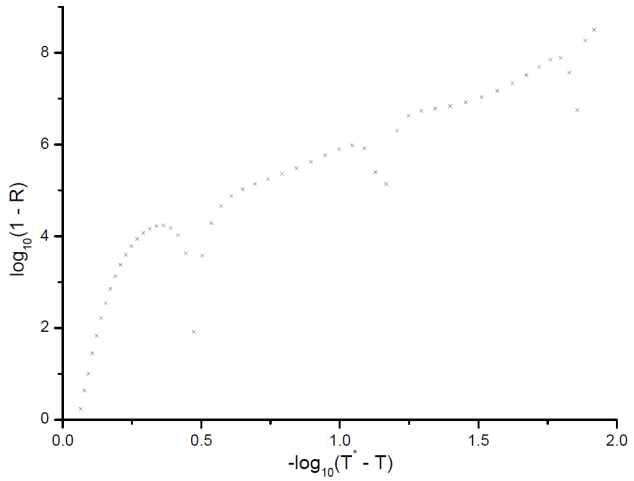

Fig. 7.4.22 Ricci curvature R on axis in terms of $\tau = -\log_{10}(T^* - T)$ for $\Lambda = 0$.

The evolution of the Ricci curvature scalar R is visualised in figure 7.4.22. As it is evident from equation 7.30, its value increases with each field oscillation. Since we expect an infinite number of peaks, the Ricci curvature probably grows without bound in a region close to the axis. The field energy density on axis in terms of Ricci is

$$\rho(u,u) = \frac{p^2}{4\pi G a^2} = -\frac{R}{32\pi G}. \tag{7.31}$$

Thus, in strong field regions the density ρ also becomes arbitrarily large.

7.4.3 Strong field regions at far distance

An interesting question is whether these regions are observed at far distance. For an observer sitting at constant area radius r, equation 7.29 generalises to

$$T(u, r = const) = \int_0^u a(x, v(x,r)) \sqrt{\left.\frac{\partial v}{\partial u}\right|_r}\, \mathrm{d}x. \tag{7.32}$$

This integral clearly diverges in the supercritical case due to the formation of an apparent horizon. However, the proper time does not become arbitrarily large for subcritical initial data, which is in contrast to what one might expect due to continuity.

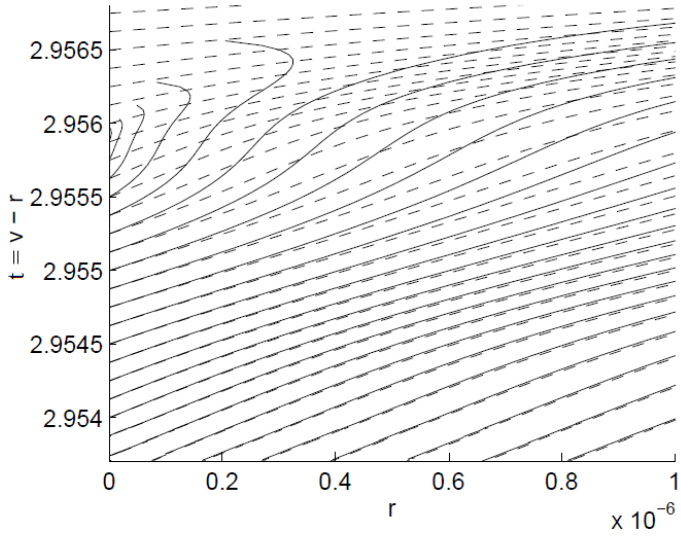

Fig. 7.4.3 Light cone structure in quasi-Eddington-Finkelstein coordinates for *marginally* subcritical (dashed) and supercritical (solid) data which differ by one part in 10^{15}. (taken from [21])

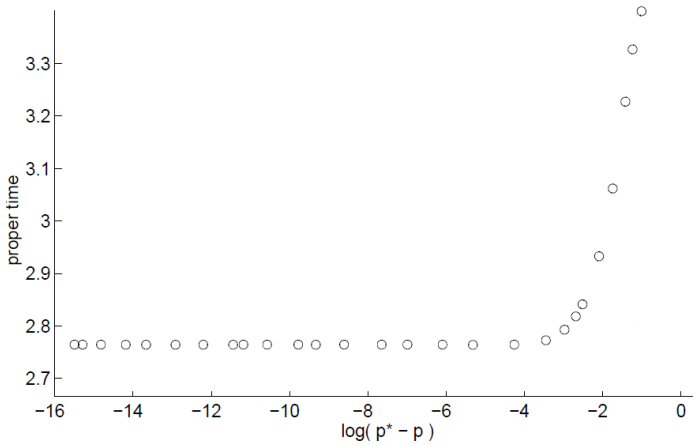

Fig. 7.4.31 Proper time required to reach an observer at constant $r = 0.1$ in terms of $\log_{10}(p^* - p)$ for subcritical initial data where u is specified to 3.4. (taken from [21])

The null cone structure of subcritical and supercritical solutions is compared in [21]. By performing a series of evolutions, the critical parameter p is determined with an accuracy of one part in 10^{15}. Figure 7.4.3 depicts the evolution for both choices of initial data in ingoing quasi-Eddington-Finkelstein coordinates with constant u-spacing. While the solutions agree with each other at the beginning, the late time behaviour is different. In the supercritical case light cones change direction

and return to $r = 0$ due to the formation of the horizon. Thus, photons can not escape and are not seen by a distant observer. In the subcritical case, however, lines do not turn around, but the slope descends. This is *not* what a continuity argument would suggest and as a consequence strong field regions reach a distant observer located at fixed r in *finite* proper time. Figure 7.4.31 confirms this statement. Even in the $p \to p^*$ limit, the proper time measured at $r = 0.1$ remains finite.

7.4.4 Critical phenomena

In chapter 2 it was thoroughly discussed that universal phenomena occur for field configurations close to p^*. In this subsection we give concrete examples in which the maximum Ricci curvature scalar and the black hole mass obey a power law with an exponent independent of the black hole family. For the former case, the evolution is simulated twice using different initial field configurations on the $C_+(u = 0, v)$ cone. In figure 7.4.4 the initial Gaussian curve $\exp\left[-10^4\left(h_n - \frac{h_{max}}{4h_n}\right)^2\right]$ is compared to the second initial field configuration $h_n^{-5}\left[\exp\left(\frac{1}{h_n} - 1\right)\right]^{-1}$, where $h_n = nh$.

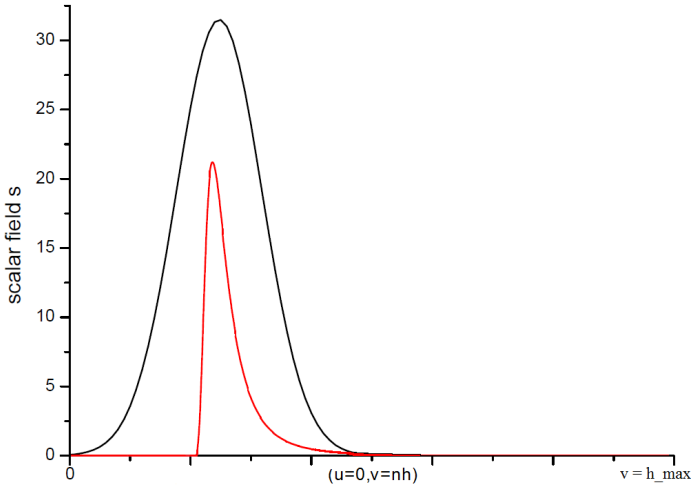

Fig. 7.4.4 Initial field configuration on the null cone $C_+(u = 0, v)$. The Gaussian curve (black) is $\exp\left[-10^4\left(h_n - \frac{h_{max}}{4h_n}\right)^2\right]$. The red curve depicts $h_n^{-5}\left[\exp\left(\frac{1}{h_n} - 1\right)\right]^{-1}$.

We focus on *marginally subcritical* solutions and determine the maximum Ricci curvature scalar R_{max} in terms of the aberration from the threshold. Figure 7.4.41 shows a linear relationship in double $\log_{10}$ scale with a *universal* slope of $k_1 = -0.751$ for Gaussian initial data and $k_2 = -0.768$ for the second choice of initial data. This confirms that for fine-tuned initial data the maximum curvature scales as [16, 20]

$$R_{max} = L\,(p^* - p)^{2\gamma}\,. \tag{7.33}$$

As it will be soon revealed in more detail, the numerical value of γ is approximately 0.374 and thus agrees with our result.

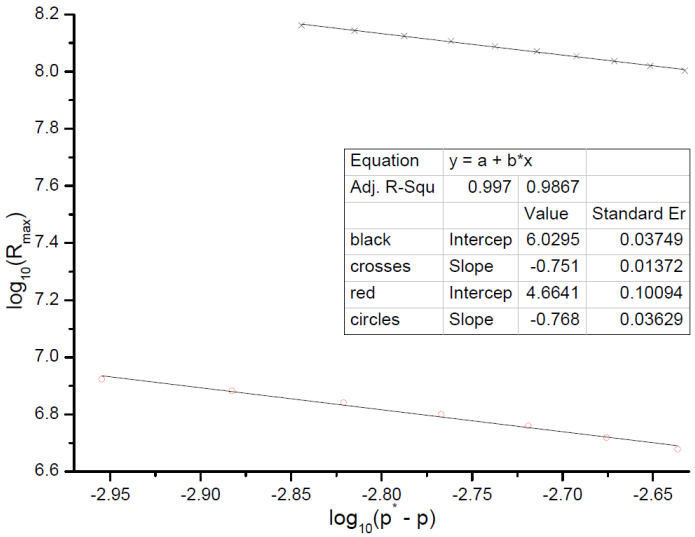

Fig. 7.4.41 Maximum curvature R_{max} in terms of $(p^* - p)$ in double $\log_{10}$ scale for subcritical Gaussian (black crosses) and exp $\left[-10^4 \left(h_n - \frac{h_{max}}{4h_n}\right)^2\right]$ (red circles) initial data. The straight lines were determined by the least square method and have approximately slope -0.76.

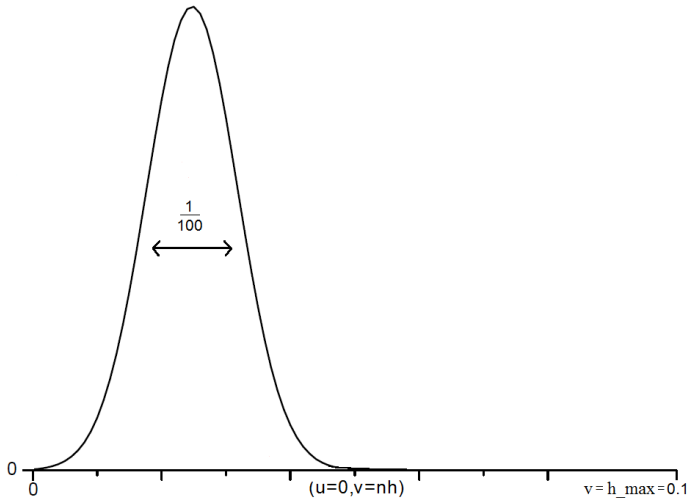

Fig. 7.4.42 The width of the Gaussian initial data is $\frac{1}{100}$. The maximum coordinate range is 0.1

Before checking the implication of a non-negative cosmological constant on the scaling behaviour, the size of Λ should be characterised. We work on a uniform grid with 100 points and distance $h = 10^{-3}$. Thus, the coordinate range is 0.1. The Gaussian initial data $\exp\left[-10^4\left(h_n - \frac{h_{max}}{4h_n}\right)^2\right]$ has width $\frac{1}{100}$, which fixes the order of magnitude of the curvature length. Since $\Lambda \sim R^{-2}$, a cosmological constant of 100 means a radius of 0.1. In conclusion, $\Lambda \sim 100$ is about the right scale. Whilst not being too large, the cosmological constant clearly changes the patch we are taking.

To explore the scaling behaviour of the curvature in case of a non-negative cosmological constant, we have to adjust the amplitude p of the Gaussian initial data due to a shift of the threshold value p^*. Figure 7.4.43 shows the maximum curvature R_{max} dependent on the same aberration from the threshold as before for a positive ($\Lambda = 100$, black crosses) and negative ($\Lambda = -100$, red circles) cosmological constant. In double $\log_{10}$ scale, the linear regression functions approximately have slope $k_3 = -0.71$ and $k_4 = -0.73$. Taking the uncertainties into account (e.g. a non-accurate value of p^*), this confirms that the critical exponent γ does not depend on Λ. This is what we expect from the phase space picture of critical phenomena. At criticality the cosmological constant is irrelevant.

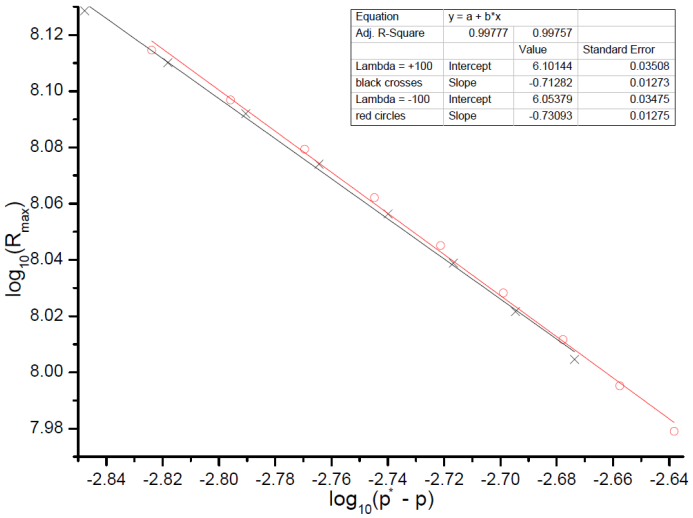

Fig. 7.4.43 Maximum curvature R_{max} in double $\log_{10}$ scale for Gaussian initial data with the same aberration from the threshold as in figure 7.4.41 ($\Lambda \neq 0$). The slopes of the straight lines for $\Lambda = 100$ (black crosses) and $\Lambda = -100$ (red circles) suggest that the critical exponent γ is independent of the cosmological constant.

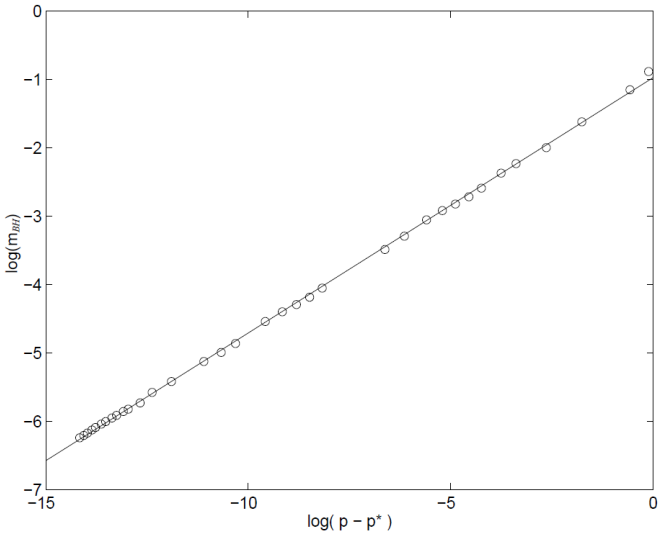

Fig. 7.4.44 Black hole mass m_{BH} in terms of $\log_{10}(p - p^*)$ for supercritical initial data. The straight line was determined by the least square method and has slope $\gamma = 0.374$. (taken from [21])

We have so far avoided a detailed discussion of supercritical solutions; primarily because it is challenging to achieve accurate results. However, a quantity that has to be discussed in the context of universality is the black hole's Hawking mass

$$m_{BH}(u_0, v_0) = \frac{r}{2}\left(1 + \frac{4fg}{a^2}\right). \tag{7.34}$$

For slightly supercritical solutions, the formation of an apparent horizon is indicated by $g = r_v$ going towards zero. For each fixed v_0, the value of u_0 is chosen such that the apparent horizon intersects with the point (u_0, v_0). However, this is not as simple as it seems to be. Computations so close to the black hole threshold are challenging. In near proximity to p^* the computer can run out of memory before the late time evolution is resolved. While our code does not achieve the required accuracy, Hamadé and Stewart locate p^* up to one part in 10^{15} and then determine the point (u_0, v_0). Figure 7.4.44 depicts the Hawking mass m_{BH} in terms of the deviation from the threshold. A straight line with slope $\gamma = 0.374$ in double $\log_{10}$ scale is a good approximation. This confirms Choptuik's conclusion in [9, 10] that black hole masses follow a power law $m_{BH} = K(p - p^*)^\gamma$, where γ is a *universal* constant. K is constant as well and only depends on the family of the black hole.

There exist three independent results for the numerical value of γ. Choptuik obtained $\gamma \approx 0.37$ using a metric in (t, r) coordinates. Figure 7.4.44 yields $\gamma \approx 0.374$. Garfinkle, who used null coordinates, computed $\gamma \approx 0.38$. The reason why we quote all three numerical values is that Kaiser [24] indicated the closeness of γ to $\frac{1}{e} = 0.367$. Choptuik did not find any theoretical explanation that supports this suggestion. Since we now have three slightly higher values, a numerical agreement is

also unlikely.

We close this chapter with the remark that its concept was inspired by Hamadé and Stewart. Their work in [21] enabled us to do genuine numerical simulations despite the limited time available. While key results could be reproduced with our code, precise solutions for highly-critical initial data require time and effort beyond the means of this dissertation. This is why we also presented figures taken from [21]. We have extended the discussion to Einstein's equations with cosmological constant Λ and thus created a link to the collapse in anti-de Sitter space.

8 Conclusion

We first summarise results of the gravitational collapse of a spherically symmetric massless scalar field discovered in this dissertation. The second section then discusses possible extensions and future work. Since it is a good preparation for the gravitational collapse in anti-de Sitter space, we begin by reviewing the findings of the implementation of a gravitational collapse in Minkowski space.

The code proposed in [21] is extended to include a cosmological constant in Einstein's equations and then implemented in MATLAB. The underlying algorithm is a second-order predictor-corrector method. Due to complexity, we do not use adapted mesh refinement. Since highly critical evolutions can only be resolved on finer grids, the simulation is therefore limited to nearly critical initial data. Except for the mass scaling behaviour, however, we succeed in reproducing (and extending some of) the results presented in [21].

We find that an initial ingoing pulse travels towards the $r = 0$ axis, bounces off and leaves to future null infinity. Depending on the critical parameter, i.e. the initial amplitude p, the scalar field either disperses or forms a black hole. We approach the critical solution by fine-tuning of initial data and observe the scalar field on axis. The field oscillates with a *universal* frequency. While the first peak depicts the initial field configuration, all further peaks are independent of initial data. The better the fine-tuning, the more oscillations are resolved. Hamadé and Stewart reveal up to 5 oscillations, the code *collapsenull* resolves 4 peaks after specifying 14 (sic!) digits beyond the decimal point. A non-negative cosmological constant shifts the threshold amplitude p^*, but does not affect the position of peaks. Thus, the universal frequency remains invariant. In addition, we compute the metric function and Ricci curvature on axis. The former goes towards zero at the singularity, the latter increases with each field oscillation. Since we expect an arbitrary number of peaks for critical initial data, we conjecture that the curvature grows without bound.

In the context of critical phenomena, the theoretical discussion suggests a universal scaling behaviour for the maximum Ricci curvature of the form

$$R_{max} \propto \left|p^* - p\right|^{2\gamma}, \tag{8.1}$$

where γ is a universal constant. This scaling behaviour should hold for both marginally subcritical and supercritical amplitudes. Except for the factor of two in the exponent, which occurs due to the quadratic length scale of curvature, similar scaling relations exist for other physical quantities like black hole charge and mass. We then compute the maximum Ricci curvature for marginally subcritical Gaussian and kink-like initial data. In double log scale, the maximum curvature depends

linearly on the aberration from the threshold. As expected, we observe a slope of $k \approx -0.76$ independent of the family of initial data. The most accurate value of the scaling exponent [21], which is determined by measuring the black hole mass for supercritical data, is $\gamma_1 = 0.374$ and thus approximately agrees with our result. After choosing a non-zero cosmological constant $\Lambda_{1,2} = \pm 100$ and carefully readjusting p^*, slopes of $k_1 = -0.71$ and $k_2 = -0.73$ are determined. This confirms that the exponent γ at criticality is independent of the cosmological constant.

We now focus on the maximally symmetric solution of Einstein's equations with negative cosmological constant. In particular due to peculiar boundary properties, a simulation of gravitational collapse in anti-de Sitter space is more challenging and extra care is required. Hence, we included an introduction to the geometry of AdS (c.f. section 4.1.1) in this dissertation. A consequence of the geometric properties is that light rays, as seen by an observer on a geodesic, travel to and bounce off the timelike boundary in finite proper time. We begin by summarising results of a collapse in 2+1 dimensional AdS *before* any reflections off the boundary.

Whilst it should be stressed that metric, coordinates and numerical scheme are adapted to the characteristics of this problem, this conclusion focuses on findings of critical phenomena. Initially, in case that an apparent horizon forms within the simulation time, the asymptotic mass is estimated at the AH. Tuning the initial field amplitude from fairly subcritical to supercritical values, suggests a universal scaling behaviour above the black hole threshold. Since the mass scaling discussion in [29] is somewhat vague, we use their numerical data to check the slope in double log scale. It turns out that the asymptotic mass roughly obeys the expected scaling relation only slightly above the threshold. The physical reason is that any non-collapsing outgoing components reflect off the AdS boundary and falsify the measurement. It is more suitable to determine the critical scaling exponent γ by measuring the maximum Ricci curvature for subcritical initial data. The exponent's value $\gamma_2 = 1.2$, which differs from γ_1 (as it should), is again independent of initial data. Larger uncertainties indicate the challenge faced in simulating a collapse in AdS. Another important result is the visualisation of continuous self-similarity. After introducing scale-invariant variables, a comparison of the field's first and second derivatives confirms that the profiles of Gaussian, Gaussian-squared and kink initial data are indistinguishable in the critical limit.

Finally, a briefer but more technical chapter discusses stability properties of AdS. While de Sitter space and Minkowski are known to be stable under small perturbations, anti-de Sitter space (with no-flux boundary conditions) is only asymptotically stable. Stability issues of gravitational collapse in AdS have not been discussed for a long time, but Bizoń and Rostworowski have recently presented notable results [6]. Their approach is similar as in [29], except for focusing on evolutions *after* reflections off the timelike AdS boundary. This requires long-term field observations at high computational cost and thus is numerically challenging. To reveal critical phenomena, the initial amplitude is tuned from above the black hole threshold before any reflection off the boundary down to weak amplitudes. The radius x_H of the apparent horizon, which forms before a collapse, is monitored before it goes to zero at a critical amplitude ϵ_0. So far nothing new, but - due to the peculiar geometry of AdS - a wave packet with $\epsilon < \epsilon_0$ travels to and bounces off the boundary.

For further decreased amplitudes, the scenario described above repeats itself and we find a series of critical amplitudes ϵ_n. In addition, the horizon radius x_H slightly above each critical amplitude scales as

$$x_H(\epsilon) \propto (\epsilon - \epsilon_n)^\gamma, \quad \gamma \approx 0.37. \tag{8.2}$$

At criticality, the scaling behaviour is not influenced by the cosmological constant and goes towards Choptuik's self-similar solution. An arbitrary number of critical amplitudes is expected in theory, which suggests a missing lower black hole threshold. However, in practice only 10 reflections off the boundary are resolved.

To explore instability of AdS, it is argued that the Ricci curvature scalar at the centre is an indicator of stability. Since we observe exponential growth for weak initial data, which can not be cured by a rescaling of $\epsilon^{-2}R(\epsilon^2 t, 0)$, instability is expected. A more rigorous understanding is developed by applying weakly nonlinear perturbations to the metric variables. While at first order solutions of the resultant differential equations are stable, at higher orders resonant terms occur and lead to unremovable secular terms causing instability. In analogy to the nonlinear Schrödinger equation on a torus, it is found that this instability is connected with a shift of energy towards higher frequencies.

8.1 Extensions and future work

Regarding future work, the first thing to do is to enhance the self-written code. Probably, minor improvements of the treatment of boundary conditions on the $r = 0$ axis are possible. In addition, the rearrangement of the implicit equation 7.25 in the predictor step of the two-variable scheme into an explicit form should be checked. This step is not at all described in [21], and there are arbitrary ways to deal with it. However, it is more important to add adaptive mesh refinement [5] to the code. Owing to the results in the original paper, we expect significant improvements, especially in proximity of the black hole threshold. The downside is that the implementation of adaptive refinement is rather challenging. Since numerical results in [21] have high precision, introducing auxiliary variables to rewrite Einstein's equations as a set of first-order differential equations proved to be effective. Even though success is not guaranteed, a similar code for the gravitational collapse in AdS would be a nice piece of future work.

Regarding critical phenomena in AdS collapse, the appearance has been experimentally confirmed. However, in theory a critical solution is yet to be found. In particular, it is unclear what kind of symmetry occurs at criticality. A global homothetic Killing vector is not consistent with Einstein's field equations with $\Lambda \neq 0$. Furthermore, the critical solution is expected to be one-mode unstable, but experimental evidence is still missing. In addition, consequences of the reflecting timelike boundary should be explored in more detail. E.g., will any field configuration with an asymptotic mass $M > 0$ eventually form a black hole? Even though notable results suggesting AdS instability exist, the influence of the cosmological constant is not fully understood. On the one hand Λ could only limit the evolution to within the boundary, or more importantly the cosmological constant may be controlling instability. Lastly, an understanding of critical phenomena in the

context of the AdS_{d+2}/CFT_{d+1} would be interesting.

The final but obvious extension of this dissertation is to include other types of matter in the discussion, e.g. perfect fluids or massive complex scalar fields. This should go along with a broader analysis of critical phenomena, which are much more general than presented in this dissertation.

Bibliography

[1] Aharony and Gubser and Maldacena and Ooguri and Oz, *Large N Field Theories, String Theory and Gravity*, Physics Reports **323** (1999), 261.

[2] Michael T Anderson, *On the uniqueness and global dynamics of AdS spacetimes*, Class Quantum Grav **23** (2006), 18.

[3] Thomas W Baumgarte and Stuart L Shapiro, *Numerical Relativity: Solving Einstein's Equations on the Computer*, Cambridge University Press, United Kingdom, 2010.

[4] Ingemar Bengtsson, *Anti-de Sitter Space*, Lecture notes, 1998.

[5] Marsha J Berger and Joseph Oliger, *Adaptive mesh refinement for hyperbolic partial differential equations*, Journal of Computational Physics **53** (1984), 29.

[6] Piotr Bizoń and Andrzej Rostworowski, *Weakly turbulent instability of anti-de Sitter space*, Physical Review Letters **107** (2011), 4.

[7] Lior M Burko, *Singularity in 2+1 dimensional AdS-scalar black hole*, Physical Review D **62** (2000), 4.

[8] Rémi Carles and Erwan Faou, *Energy cascades for NLS on the torus*, Math Appl (2010), 15.

[9] Matthew W Choptuik, *Universality and scaling in gravitational collapse of a massless scalar field*, Physical Review Letters **70** (1992), 4.

[10] ———, *Critical behaviour in a scalar field collapse*, Cambridge University Press, United Kingdom, 1992.

[11] ———, *http://godel.ph.utexas.edu:80/Ftp/critfmt/*.

[12] Demetrios Christodoulou, *The formation of black holes and singularities in spherically symmetric gravitational collapse*, Comm Pure Appl Math **44** (1991), 35.

[13] ———, *Bounded variation solutions of the spherically symmetric einstein-scalar field equations*, Comm Pure Appl Math **46** (1993), 90.

[14] Colliander and Keel and Staffilani and Takaoka and Tao, *Transfer of energy to high frequencies in the cubic defocusing nonlinear Schrödinger equation*, Invent Math **181** (2010), 75.

[15] David Garfinkle, *Choptuik scaling in null coordinates*, Physical Review D **51** (1994), 4.

[16] David Garfinkle and Corner G Duncan, *Scaling of curvature in sub-critical gravitational collapse*, Physical Review D **58** (1998), 6.

[17] Carsten Gundlach, *The Choptuik spacetime as an eigenvalue problem*, Physical Review Letters **75** (1995), 5.

[18] ———, *Understanding critical collapse of a scalar field*, Physical Review D **55** (1997), 26.

[19] ———, *Global structure of Choptuiks critical solution in scalar field collapse*, Physical Review D **68** (2003), 25.

[20] Carsten Gundlach and José M Martín-García, *Critical phenomena in gravitational collapse*, Physics Reports **376** (2003), 66.

[21] Rufus S Hamadé and John M Stewart, *The spherically symmetric collapse of a massless scalar field*, Class Quantum Grav **13** (1995), 23.

[22] Stephen W Hawking and George F R Ellis, *The Large Scale Structure of Space-Time*, Cambridge University Press, United Kingdom, 1975.

[23] Viqar Husain and Michel Olivier, *Scalar field collapse in three-dimensional AdS spacetime*, Class Quantum Grav **18** (2000), 10.

[24] Nick Kaiser, *Private communication with Matthew W Choptuik*.

[25] Heinz Kreiss and Joseph Oliger, *Methods for the approximate solution of time dependent problems*, Global Atmospheric Research Programme **10** (1973), 107.

[26] Juan M Maldacena, *The Large N limit of superconformal field theories and supergravity*, Theor Math Phys **2** (1998), 22.

[27] Alexander Ostermann, *Numerische Mathematik 1*, Lecture notes, 2010.

[28] Press and Teukolsky and Vetterling and Flannery, *Numerical Recipes 3rd Edition: The Art of Scientific Computing*, Cambridge University Press, United States of America, 2007.

[29] Frans Pretorius and Matthew W Choptuik, *Gravitational collapse in 2+1 dimensional AdS spacetime*, Physical Review D **62** (2000), 31.

[30] Robert M Wald, *General Relativity*, University of Chicago Press, United States of America, 1984.

A Annex

A.1 MATLAB codes

```
function int = gaussian_order5(fun)

%Gaussian_order5 computes the integral of a function over the interval
%[0,1] by using the Gaussian quadrature rule of order 5.

%input:
            %fun: integrand (function)

%output:
            %int: approximation of the integral using the Gaussian
            %quadrature rule of order 5.

x = [1/2-sqrt(15)/10,1/2,1/2+sqrt(15)/10]; %integration points
y = fun(x);                                %function values at these points

int = 1/18*(5*y(1)+8*y(2)+5*y(3));     %Gaussian quadrature rule of order 5

end
```

```
function erg = collapse_cosm_const(max,h,lambda)

%Simulation of the spherically symmetric collapse of a massless scalar
%field using a first order explicit method (Euler scheme). The Einstein
%equations include a cosmological constant lambda.

%input:
            %max: # of grid-points in u,v - direction
            %h: step size
            %lambda: cosmological constant

%output:
            %mesh(uarr,varr,s): 3-D mesh surface plot; s is scalar field
            %erg: metric function a on u = v axis

imax = max;
```

```
for i = 1:max                       %constructs grid in u and v direction

    uarr(i,1:max) = (i-1)*h;
    varr(1:max,i) = (i-1)*h;

end

%each matrix corresponds to the value of the variable on the grid

a = zeros(max,max);
d = zeros(max,max);
f = zeros(max,max);
g = zeros(max,max);
p = zeros(max,max);
q = zeros(max,max);
r = zeros(max,max);
s = zeros(max,max);

%initial field configuration
s(1,1:max) =  3.14445*10^(-1)*exp(-10^4*((0:h:(max-1)*h)-max/4*h).^2);

%\frac{df}{dv}|(u=0,v)
q(1,1:max) = -2*3.14445*10^(3)*((0:h:(max-1)*h)-max/4*h).* ...
.*exp(-10^4*((0:h:(max-1)*h)-max/4*h).^2);

%inital values on (u=0,v=0)
a(1,1) = 1;
p(1,1) = q(1,1);
g(1,1) = 1/2*a(1,1);
f(1,1) = -1/2*a(1,1);

%assigns minor value of r on u=v axis to avoid singularity
for k = 1:max

    r(k,k) = 10^(-5);

end

for i = 2:imax          %solution on (u=0,v)

    a(1,i) = a(1,i-1)+h*a(1,i-1)*d(1,i-1);
    r(1,i) = r(1,i-1)+h*g(1,i-1);
    g(1,i) = g(1,i-1)+h*(2*d(1,i-1)*g(1,i-1)-r(1,i-1)*q(1,i-1)^2);
    f(1,i) = f(1,i-1)-h*(f(1,i-1)*g(1,i-1)+1/4*a(1,i-1)^2)/r(1,i-1)+...
    +h/4*lambda*r(1,i-1)*a(1,i-1)^2; %due to cosmological constant
    p(1,i) = p(1,i-1)-h*(f(1,i-1)*q(1,i-1)+g(1,i-1)*p(1,i-1))/r(1,i-1);

end

for j = 2:max-1    %solution on the remaining grid (u less or equal than v)
```

```
for i = 1:imax-1

    %values on (u,u) with first order approximation
    if (i == 1) && ((j == 2) || (j == max-1))

        %\frac{da}{dr}|(u,u) = 0 as first order approximation
        a(j,j) = a(j-1,j+1);
        %\frac{ds}{dr}|(u,u) = 0 as first order approximation
        s(j,j) = s(j-1,j+1);
        g(j,j)=1/2*a(j,j);
        f(j,j)=-1/2*a(j,j);

        q(j,i+j-1) = q(j-1,i+j-1)-h*(f(j-1,i+j-1)*q(j-1,i+j-1)+...
        +g(j-1,i+j-1)*p(j-1,i+j-1))/r(j-1,i+j-1);
        d(j,i+j-1) = d(j-1,i+j-1)+h*((f(j-1,i+j-1)*g(j-1,i+j-1)+...
        +1/4*a(j-1,i+j-1)^2)/r(j-1,i+j-1)^2-p(j-1,i+j-1)*q(j-1,i+j-1));
        p(j,j) = q(j,j);

    %values on (u,u) with second order approximation
    elseif i == 1

        %\frac{da}{dr}|(u,u) = 0 as second order approximation
        a(j,j) = 1/3*(4*a(j-1,j+1)-a(j-2,j+2));
        %\frac{ds}{dr}|(u,u) = 0 as second order approximation
        s(j,j) = 1/3*(4*s(j-1,j+1)-s(j-2,j+2));
        g(j,j)=1/2*a(j,j);
        f(j,j)=-1/2*a(j,j);

        q(j,i+j-1) = q(j-1,i+j-1)-h*(f(j-1,i+j-1)*q(j-1,i+j-1)+...
        +g(j-1,i+j-1)*p(j-1,i+j-1))/r(j-1,i+j-1);
        d(j,i+j-1) = d(j-1,i+j-1)+h*((f(j-1,i+j-1)*g(j-1,i+j-1)+...
        +1/4*a(j-1,i+j-1)^2)/r(j-1,i+j-1)^2-p(j-1,i+j-1)*q(j-1,i+j-1));
        p(j,j) = q(j,j);

    else

        q(j,i+j-1) = q(j-1,i+j-1)-h*(f(j-1,i+j-1)*q(j-1,i+j-1)+...
        g(j-1,i+j-1)*p(j-1,i+j-1))/r(j-1,i+j-1);
        d(j,i+j-1) = d(j-1,i+j-1)+h*((f(j-1,i+j-1)*g(j-1,i+j-1)+...
        +1/4*a(j-1,i+j-1)^2)/r(j-1,i+j-1)^2-p(j-1,i+j-1)*q(j-1,i+j-1));

        a(j,i+j-1) = a(j,i+j-2)+h*a(j,i+j-2)*d(j,i+j-2);
        r(j,i+j-1) = r(j,i+j-2)+h*g(j,i+j-2);
        g(j,i+j-1) = g(j,i+j-2)+h*(2*d(j,i+j-2)*g(j,i+j-2)-...
        -r(j,i+j-2)*q(j,i+j-2)^2);
        s(j,i+j-1) = s(j,i+j-2)+h*q(j,i+j-2);
        f(j,i+j-1) = f(j,i+j-2)-h*(f(j,i+j-2)*g(j,i+j-2)+...
        +1/4*a(j,i+j-2)^2)/r(j,i+j-2)+...
        +h/4*lambda*r(j,i+j-2)*a(j,i+j-2)^2; %due to cosmolog. constant
```

```
            p(j,i+j-1) = p(j,i+j-2)-h*(f(j,i+j-2)*q(j,i+j-2)+...
            +g(j,i+j-2)*p(j,i+j-2))/r(j,i+j-2);

        end

    end

imax = imax-1;

end

mesh(uarr,varr,s);    % 3-D mesh surface plot

erg = diag(a);

%run: collapse_cosm_const(100,10^(-3),0)

end


function erg = collapse2(max,h)

%Simulation of the spherically symmetric collapse of a massless scalar
%field using a second order explicit method with predictor-corrector.

%input:
            %max: # of grid-points in u,v - direction
            %h: step size

%output:
            %mesh(uarr,varr,s): 3-D mesh surface plot; s is scalar field

for i = 1:max                    %constructs grid in u and v direction

    uarr(i,1:max) = (i-1)*h;
    varr(1:max,i) = (i-1)*h;

end

%each matrix corresponds to the value of the variable on the grid

a = zeros(max,max);
d = zeros(max,max);
f = zeros(max,max);
g = zeros(max,max);
p = zeros(max,max);
q = zeros(max,max);
r = zeros(max,max);
s = zeros(max,max);
```

```
%initial field configuration
s(1,1:max) = 10^(-1)*exp(-10^4*((0:h:(max-1)*h)-max/4*h).^2);

%\frac{df}{dv}|(u=0,v)
q(1,1:max) = -2*10^(3)*((0:h:(max-1)*h)-max/4*h).*...
    .*exp(-10^4*((0:h:(max-1)*h)-max/4*h).^2);

%inital values on (u=0,v=0)
a(1,1) = 1;
p(1,1) = q(1,1);
g(1,1) = 1/2*a(1,1);
f(1,1) = -1/2*a(1,1);


%assigns minor value of r on u=v axis to avoid singularity
for k = 1:max

    r(k,k) = 10^(-5);

end

for i = 2:max          %solution on (u=0,v)

    a(1,i) = a(1,i-1)+h*a(1,i-1)*d(1,i-1);
    r(1,i) = r(1,i-1)+h*g(1,i-1);
    g(1,i) = g(1,i-1)+h*(2*d(1,i-1)*g(1,i-1)-r(1,i-1)*q(1,i-1)^2);
    f(1,i) = f(1,i-1)-h*(f(1,i-1)*g(1,i-1)+1/4*a(1,i-1)^2)/r(1,i-1);
    p(1,i) = p(1,i-1)-h*(f(1,i-1)*q(1,i-1)+g(1,i-1)*p(1,i-1))/r(1,i-1);

end



b = 0;

for j = 2:max      %solution on the remaining grid (u less or equal than v)

    for i = (3+b):max

        %values on (u,u) with first order approximation
        if i == (3+b) && ((j == 2) || (j == max-1))

            %\frac{da}{dr}|(u,u) = 0 as first order approximation
            a(i-1,i-1) = a(i-2,i);
            %\frac{ds}{dr}|(u,u) = 0 as first order approximation
            s(i-1,i-1) = s(i-2,i);
            g(i-1,i-1) = 1/2*a(i-1,i-1);
            f(i-1,i-1) = -1/2*a(i-1,i-1);

            %values on (u,u) (step 0)
```

```
q(i-1,i-1) = q(i-2,i-1)-h*(f(i-2,i-1)*q(i-2,i-1)+...
+g(i-2,i-1)*p(i-2,i-1))/r(i-2,i-1);
d(i-1,i-1) = d(i-2,i-1)+h*((f(i-2,i-1)*g(i-2,i-1)+...
+1/4*a(i-2,i-1)^2)/r(i-2,i-1)^2-p(i-2,i-1)*q(i-2,i-1));
p(i-1,i-1) = q(i-1,i-1);

%predicted values in u - direction (step 1)
q(j,i) = q(j-1,i)-h*(f(j-1,i)*q(j-1,i)+g(j-1,i)*...
*p(j-1,i))/r(j-1,i);
d(j,i) = d(j-1,i)+h*((f(j-1,i)*g(j-1,i)+1/4*a(j-1,i)^2)/...
/r(j-1,i)^2-p(j-1,i)*q(j-1,i));

%predicted values in v - direction (step 2)
a(j,i) = (a(j,i-1)+1/2*h*a(j,i-1)*d(j,i-1))/(1-1/2*h*d(j,i));
r(j,i) = -(2*d(j,i-1)*g(j,i-1)*h^2 - 2*d(j,i)*h*...
*(g(j,i-1)*h+2*r(j,i-1))+4*g(j,i-1)*h-r(j,i-1)*...
*(h^2*q(j,i-1)^2-4))/(4*d(j,i)*h-h^2*q(j,i)^2-4);
s(j,i) = s(j,i-1)+1/2*h*(q(j,i-1)+q(j,i));
g(j,i) = -(4*d(j,i-1)*g(j,i-1)*h + g(j,i-1)*...
*(4-h^2*q(j,i)^2)-2*h*r(j,i-1)*(q(j,i-1)^2+q(j,i)^2))/...
/(4*d(j,i)*h-h^2*q(j,i)^2-4);
f(j,i) = -(a(j,i-1)^2*h*r(j,i)+4*f(j,i-1)*r(j,i)*(g(j,i-1)*h...
-2*r(j,i-1))+h*r(j,i-1)*a(j,i)^2)/(4*r(j,i-1)*...
*(h*g(j,i)+2*r(j,i)));
p(j,i) = -(h*r(j,i-1)*q(j,i)*f(j,i)+r(j,i)*(f(j,i-1)*h*...
*q(j,i-1)+p(j,i-1)*(g(j,i-1)*h-2*r(j,i-1))))/...
/(r(j,i-1)*(h*g(j,i)+2*r(j,i)));

%intermediate step to save predicted values (in u-direction)
q_old = q(j,i);
d_old = d(j,i);

a_old = a(j,i);
r_old = r(j,i);
g_old = g(j,i);
f_old = f(j,i);

%corrected values in u - direction (step 3)
q(j,i) = 1/2*(q_old+q(j-1,i)-h*(f(j,i)*...
*q(j,i)+g(j,i)*p(j,i))/r(j,i));                    %yn
d(j,i) = 1/2*(d_old+d(j-1,i)+h*((f(j,i)*g(j,i)+...
+1/4*a(j,i)^2)/r(j,i)^2-p(j,i)*q_old));

%corrected values in v - direction (step 4)
a(j,i) = 1/2*(a(j,i)+a(j,i-1)+h*a(j,i)*d_old);
r(j,i) = 1/2*(r_old+r(j,i-1)+h*g(j,i));
s(j,i) = 1/2*(s(j,i)+s(j,i-1)+h*q_old);
g(j,i) = 1/2*(g_old+g(j,i-1)+h*(2*d_old*g_old-r_old*q_old^2));
f(j,i) = 1/2*(f_old+f(j,i-1)-h*(f_old*g_old+1/4*a_old^2)/r_old)
p(j,i) = 1/2*(p(j,i)+p(j,i-1)-h*(f_old*q_old+g_old*p(j,i))/...
```

```
    /r_old);

%values on (u,u) with second order approximation
elseif i == (3+b)

    %\frac{da}{dr}|(u,u) = 0 as second order approximation
    a(i-1,i-1) = 1/3*(4*a(i-2,i)-a(i-3,i+1));
    %\frac{ds}{dr}|(u,u) = 0 as second order approximation
    s(i-1,i-1) = 1/3*(4*s(i-2,i)-s(i-3,i+1));
    g(i-1,i-1) = 1/2*a(i-1,i-1);
    f(i-1,i-1) = -1/2*a(i-1,i-1);

    %values on (u,u) (step 0)
    q(i-1,i-1) = q(i-2,i-1)-h*(f(i-2,i-1)*q(i-2,i-1)+...
    +g(i-2,i-1)*p(i-2,i-1))/r(i-2,i-1);
    d(i-1,i-1) = d(i-2,i-1)+h*((f(i-2,i-1)*g(i-2,i-1)+...
    +1/4*a(i-2,i-1)^2)/r(i-2,i-1)^2-p(i-2,i-1)*q(i-2,i-1));
    p(i-1,i-1) = q(i-1,i-1);

    %predicted values in u - direction (step 1)
    q(j,i) = q(j-1,i)-h*(f(j-1,i)*q(j-1,i)+g(j-1,i)*...
    *p(j-1,i))/r(j-1,i);
    d(j,i) = d(j-1,i)+h*((f(j-1,i)*g(j-1,i)+1/4*a(j-1,i)^2)/...
    /r(j-1,i)^2-p(j-1,i)*q(j-1,i));

    %predicted values in v - direction (step 2)
    a(j,i) = (a(j,i-1)+1/2*h*a(j,i-1)*d(j,i-1))/(1-1/2*h*d(j,i));
    r(j,i) = -(2*d(j,i-1)*g(j,i-1)*h^2 - 2*d(j,i)*h*...
    *(g(j,i-1)*h+2*r(j,i-1))+4*g(j,i-1)*h-r(j,i-1)*(h^2*q(j,i-1)^2-4))/(4*d(j,i)*h-h^2*q(
    s(j,i) = s(j,i-1)+1/2*h*(q(j,i-1)+q(j,i));
    g(j,i) =-(4*d(j,i-1)*g(j,i-1)*h + g(j,i-1)*(4-h^2*q(j,i)^2)-...
    2*h*r(j,i-1)*(q(j,i-1)^2+q(j,i)^2))/(4*d(j,i)*h-h^2*q(j,i)^2-4)
    f(j,i) = -(a(j,i-1)^2*h*r(j,i)+4*f(j,i-1)*r(j,i)*(g(j,i-1)*h...
    -2*r(j,i-1))+h*r(j,i-1)*a(j,i)^2)/(4*r(j,i-1)*...
    *(h*g(j,i)+2*r(j,i)));
    p(j,i) = -(h*r(j,i-1)*q(j,i)*f(j,i)+r(j,i)*(f(j,i-1)*h*...
    *q(j,i-1)+p(j,i-1)*(g(j,i-1)*h-2*r(j,i-1))))/(r(j,i-1)*...
    *(h*g(j,i)+2*r(j,i)));

    %intermediate step to save predicted values (in u-direction)
    q_old = q(j,i);
    d_old = d(j,i);

    a_old = a(j,i);
    r_old = r(j,i);
    g_old = g(j,i);
    f_old = f(j,i);

    %corrected values in u - direction (step 3)
    q(j,i) = 1/2*(q_old+q(j-1,i)-h*(f(j,i)*q(j,i)+...
```

```
    +g(j,i)*p(j,i))/r(j,i));
    d(j,i) = 1/2*(d_old+d(j-1,i)+h*((f(j,i)*g(j,i)+1/...
    /4*a(j,i)^2)/r(j,i)^2-p(j,i)*q_old));

    %corrected values in v - direction (step 4)
    a(j,i) = 1/2*(a(j,i)+a(j,i-1)+h*a(j,i)*d_old);
    r(j,i) = 1/2*(r_old+r(j,i-1)+h*g(j,i));
    s(j,i) = 1/2*(s(j,i)+s(j,i-1)+h*q_old);
    g(j,i) = 1/2*(g_old+g(j,i-1)+h*(2*d_old*g_old-r_old*q_old^2));
    f(j,i) = 1/2*(f_old+f(j,i-1)-h*(f_old*g_old+1/4*a_old^2)/r_old)
    p(j,i)=1/2*(p(j,i)+p(j,i-1)-h*(f_old*q_old+g_old*p(j,i))/r_old)


else

    %predicted values in u - direction (step 1)
    q(j,i) = q(j-1,i)-h*(f(j-1,i)*q(j-1,i)+g(j-1,i)*...
    *p(j-1,i))/r(j-1,i);
    d(j,i) = d(j-1,i)+h*((f(j-1,i)*g(j-1,i)+1/4*a(j-1,i)^2)/...
    /r(j-1,i)^2-p(j-1,i)*q(j-1,i));

    %predicted values in v - direction (step 2)
    a(j,i) = (a(j,i-1)+1/2*h*a(j,i-1)*d(j,i-1))/(1-1/2*h*d(j,i));
    r(j,i) = -(2*d(j,i-1)*g(j,i-1)*h^2 - 2*d(j,i)*h*(g(j,i-1)*h+...
    +2*r(j,i-1))+4*g(j,i-1)*h-r(j,i-1)*(h^2*q(j,i-1)^2-4))/(4*d(j,i)*h-h^2*q(j,i)^2-4);
    s(j,i) = s(j,i-1)+1/2*h*(q(j,i-1)+q(j,i));
    g(j,i) = -(4*d(j,i-1)*g(j,i-1)*h + g(j,i-1)*(4-h^2*q(j,i)^2)-...
    2*h*r(j,i-1)*(q(j,i-1)^2+q(j,i)^2))/(4*d(j,i)*h-h^2*q(j,i)^2-4)
    f(j,i) = -(a(j,i-1)^2*h*r(j,i)+4*f(j,i-1)*r(j,i)*(g(j,i-1)*h...
    -2*r(j,i-1))+h*r(j,i-1)*a(j,i)^2)/(4*r(j,i-1)*...
    *(h*g(j,i)+2*r(j,i)));
    p(j,i) = -(h*r(j,i-1)*q(j,i)*f(j,i)+r(j,i)*(f(j,i-1)*h*...
    *q(j,i-1)+p(j,i-1)*(g(j,i-1)*h-2*r(j,i-1))))/(r(j,i-1)*...
    *(h*g(j,i)+2*r(j,i)));

    %intermediate step to save predicted values (in u-direction)
    q_old = q(j,i);
    d_old = d(j,i);

    a_old = a(j,i);
    r_old = r(j,i);
    g_old = g(j,i);
    f_old = f(j,i);

    %corrected values in u - direction (step 3)
    q(j,i) = 1/2*(q_old+q(j-1,i)-h*(f(j,i)*q(j,i)+...
    +g(j,i)*p(j,i))/r(j,i));
    d(j,i) = 1/2*(d_old+d(j-1,i)+h*((f(j,i)*g(j,i)+...
    +1/4*a(j,i)^2)/r(j,i)^2-p(j,i)*q_old));
```

```
            %corrected values in v - direction (step 4)
            a(j,i) = 1/2*(a(j,i)+a(j,i-1)+h*a(j,i)*d_old);
            r(j,i) = 1/2*(r_old+r(j,i-1)+h*g(j,i));
            s(j,i) = 1/2*(s(j,i)+s(j,i-1)+h*q_old);
            g(j,i) = 1/2*(g_old+g(j,i-1)+h*(2*d_old*g_old-r_old*q_old^2));
            f(j,i) = 1/2*(f_old+f(j,i-1)-h*(f_old*g_old+1/4*a_old^2)/r_old)
            p(j,i) = 1/2*(p(j,i)+p(j,i-1)-h*...
            *(f_old*q_old+g_old*p(j,i))/r_old);

        end

    end

b = b+1;

end

erg = mesh(uarr,varr,s);        % 3-D mesh surface plot

%run: collapse2(100,10^(-3))

end


%Toby Wiseman's version
%Special Topic lectures on 'Numerical Relativity'
%
%Spherical collapse - null coordinates
%
function [ uarr, varr, parr, Aarr, Barr ] = collapsenull( Nin )

global N u v du dv  p A B ;


N = Nin ;

maxu = 10. ;

u = 0:(maxu/(N-1)):maxu ;

v = u ;

du = u(2) ; dv = du ;


p = 9.591930865673*10^(-2)*(v-u(1)).^2.*exp(-2*(v-2.).^2) ;

B = 0.5*v ;

A(1) = 0 ;
```

```
for ii=2:N

    pv  = ( p(ii) - p(ii-1) )/dv ;

    Bval = 0.5*(B(ii) + B(ii-1)) ;

    A(ii) = A(ii-1) + dv*0.5*( pv*pv*Bval ) ;

end


uarr = zeros([N N]) ;
varr = zeros([N N]) ;
parr = zeros([N N]) ;
Aarr = zeros([N N]) ;
Barr = zeros([N N]) ;


uarr(1,:) = u ;
varr(1,:) = u(1) ;
parr(1,:) = p ;
Aarr(1,:) = A ;
Barr(1,:) = B ;


dval = 1.e-8 ;


sing = N ;

for ii=2:N-2


    v = u(ii) ;


    for jj=1:ii-1

    pnew(jj) = 0 ;
    Anew(jj) = 0 ;
    Bnew(jj) = 0 ;

    end


    if( ii == 2 )

    pnew(ii) = p(ii+1) ;
    Anew(ii) = log(B(ii+1)/dv) ;
```

```
 Bnew(ii) = 0 ;

 else

 pnew(ii) = 2*p(ii+1) - pold(ii+2) ;
 Anew(ii) = log(B(ii+1)/dv) ;
 Bnew(ii) = 0 ;

 end


 for jj=ii+1:N

 pnew(jj) = p(jj) ;
 Anew(jj) = A(jj) ;
 Bnew(jj) = B(jj) ;

 end

fprintf(1,' ii = %d\n',ii) ;

 for jj=ii+1:sing

     count=0 ;

     eq = [ 1 1 1 ] ;

     while( norm(eq)>1.e-10 && count<200 )

         count=count+1;

     vec00 = [ p(jj-1) A(jj-1) B(jj-1) ] ;

     vec10 = [ p(jj)   A(jj)   B(jj) ] ;

     vec01 = [ pnew(jj-1) Anew(jj-1) Bnew(jj-1) ] ;

     vec11 = [ pnew(jj)   Anew(jj)   Bnew(jj) ] ;

     [ eq(1) eq(2) eq(3) ] = update( ii, jj, vec00, vec10, vec01, vec11) ;


     linop = zeros([3 3]) ;

     for var=1:3

     tmpvec11 = vec11 ;

     tmpvec11(var) = vec11(var) - dval ;
```

```
    [ eq0(1) eq0(2) eq0(3) ] = update( ii, jj, vec00, vec10, vec01, tmpvec11) ;

    tmpvec11(var) = vec11(var) + dval ;

    [ eq1(1) eq1(2) eq1(3) ] = update( ii, jj, vec00, vec10, vec01, tmpvec11) ;

    linop(:,var) = (eq1-eq0)/dval ;

    end

    vec11 = vec11 - transpose(inv(linop)*transpose(eq)) ;

    pnew(jj) = vec11(1) ;
    Anew(jj) = vec11(2) ;
    Bnew(jj) = vec11(3) ;

    end

    if(count>100)

        fprintf(1,'\n ** Cant solve at %d\n\n',jj) ;

        sing = jj ;

    end

end

for jj=sing+1:N

       pnew(jj) = 0 ;
       Anew(jj) = 0 ;
       Bnew(jj) = 0 ;

end

uarr(ii,:) = u ;
varr(ii,:) = u(ii) ;
parr(ii,:) = pnew ;
Aarr(ii,:) = Anew ;
Barr(ii,:) = Bnew ;

pold = p ;
Aold = A ;
Bold = B ;

p = pnew ;
A = Anew ;
B = Bnew ;
```

```
end

subplot(1,3,1) ;

mesh(uarr(:,:),varr(:,:),parr(:,:))

subplot(1,3,2) ;

mesh(uarr(:,:),varr(:,:),Aarr(:,:))

subplot(1,3,3) ;

mesh(uarr(:,:),varr(:,:),Barr(:,:))

end

function [ eq1 eq2 eq3 ] = update( ii, jj, vec00, vec10, vec01, vec11 )

global N u du ;

p00 = vec00(1) ; A00 = vec00(2) ; B00 = vec00(3) ;
p10 = vec10(1) ; A10 = vec10(2) ; B10 = vec10(3) ;
p01 = vec01(1) ; A01 = vec01(2) ; B01 = vec01(3) ;
p11 = vec11(1) ; A11 = vec11(2) ; B11 = vec11(3) ;

p = 0.25*( p00 + p10 + p01 + p11 ) ;
A = 0.25*( A00 + A10 + A01 + A11 ) ;
B = 0.25*( B00 + B10 + B01 + B11 ) ;

pv = 0.5*( ( p10 - p00 ) + ( p11 - p01 ) )/du ;
Av = 0.5*( ( A10 - A00 ) + ( A11 - A01 ) )/du ;
Bv = 0.5*( ( B10 - B00 ) + ( B11 - B01 ) )/du ;

pu = 0.5*( ( p01 - p00 ) + ( p11 - p10 ) )/du ;
Au = 0.5*( ( A01 - A00 ) + ( A11 - A10 ) )/du ;
Bu = 0.5*( ( B01 - B00 ) + ( B11 - B10 ) )/du ;

pvu = ( p11 - p10 - p01 + p00 )/(du*du) ;
Avu = ( A11 - A10 - A01 + A00 )/(du*du) ;
Bvu = ( B11 - B10 - B01 + B00 )/(du*du) ;

eq1 = pvu + (Bv*pu + Bu*pv)*power(B,-1) ;

eq2 = Avu + (2*pu*pv - (4*Bu*Bv + exp(2*A))*power(B+du^2,-2))/4. ;

eq3 = Bvu + ((4*Bu*Bv + exp(2*A))*power(B+du^2,-1))/4. ;

end
```

```
function int = trapezoidal_rule_propertime(a,h)

%Trapezoidal_rule_propertime computes the proper time T experienced by an
%observer moving along the u = v axis by integrating the metric function
%'a' on axis using the trapezoidal rule.

%input:
            %a: values of the metric function on axis [diag(a)]; can be
            %computed by running a = collapse1(100,h)
            %h: step size of u-v grid

%output:
            %int: proper time T experienced by an observer moving along the
            %u = v axis

int(length(a)) = 0;

int(1) = sqrt(2)*h*a(1);

for j = 2:length(a)

    int(j) = 1/sqrt(2)*h*(a(j-1)+a(j))+int(j-1);  %trapezoidal rule

end

end
```